Journal of Molecular Structure 1360 (2026) 145636

Contents lists available at ScienceDirect

Journal of Molecular Structure

journal homepage: www.elsevier.com/locate/molstr

Anti-cancer and dual inhibitory potential of PI3K/AKT and Ras/MAPK/ERK signalling of a novel zinc (II) trinuclear complex with tetradentate schiff base ligand and azido ion in prostate adenocarcinoma: synthesis, *in silico* and *in vitro* evaluation

Abdul Wasai [a], Adhiraj Roy [a,*], Mamata Barua [b,1], Pameli Ghosh [c,1], Anjali Saxena [d,1], Yassir Boulaamane [e,1], Nainee Goyal [f,1], Anshuman Chandra [g,1], Subrata Nath Koner [c], Sandip Saha [b,***], Biswajit Saha [d], Subrata Kumar Pore [a], Corrado Rizzoli [h], Supratim Mandal [i,**]

[a] *Amity Institute of Molecular Medicine & Stem Cell Research, Amity University, Sector 125, Noida, Uttar Pradesh, 201303, India*
[b] *Department of Chemistry, Acharya Prafulla Chandra College, New Barrackpore, Kolkata, 700131, India.*
[c] *Department of Chemistry, Jadavpur University, Kolkata 700032, India.*
[d] *Amity Institute of Biotechnology, Amity University, Sector 125, Noida, Uttar Pradesh-201303, India*
[e] *Laboratory of Innovative Technologies, National School of Applied Sciences of Tangier, Abdelmalek Essaadi University, Tetouan, Morocco*
[f] *School of Biotechnology, Gautam Buddha University, Greater Noida, India*
[g] *School of Physical Sciences, Jawaharlal Nehru University, New Delhi, India*
[h] *Universitá degli Studi di Parma, Dipartimento S.C.V.S.A., Parco Area delle Scienze 17/A, 43124 Parma, Italy*
[i] *Department of Microbiology, University of Kalyani, Kalyani, Nadia, West Bengal 741235, India*

A R T I C L E I N F O

Keywords:
Schiff Base
Drug synthesis
Molecular docking
ADMET
PI3K/AKT and MAPK signalling
Prostate cancer therapeutics

A B S T R A C T

Background: : Prostate adenocarcinoma (PAC), especially metastatic, castration-resistant (mCRPC) ranks second most common cause of cancer-related deaths in men worldwide. Despite development of several improved treatments including PSMA-targeted radioligand therapy, mCRPC remains largely unmanageable due to chemoresistance and high relapse rate. Hence, identification of novel druggable targets and development of novel therapeutic interventions are highly warranted to improve patient outcomes.
Novelty: : A novel azido trinuclear zinc (II) Schiff base complex [{ZnL(N_3)}$_2$ Zn]. H_2O (1) (Compound AR1, abbreviated ComAR1) was synthesized using NaN_3, methanolic solution of Zn $(CH_3COO)_2.2H_2O$ and Schiff base ligand H_2L derived from condensation of 1,4-butadiamine and 3-methoxy salicylaldehyde (O-valine) at 1:2 ratio.
Results: : ComAR1 suppressed PAC cell proliferation, EMT, migration and induced G0/G1 cell cycle arrest following apoptosis. Molecular docking, simulation and ADMET analyses revealed that ComAR1 interacted with key components of signalling circuits associated with tumorigenesis including H-Ras, AKT, ERK1/2, exhibited excellent pharmacokinetic and drug-like features. Mechanistically, ComAR1 dampened PI3K/AKT and Ras/MAPK/ERK signalling activation, stabilized pro-apoptotic BAD by suppressing its AKT- and ERK-mediated phosphorylation in PAC cells.
Conclusion: : Taken together, our results indicate that ComAR1 could emerge as a novel, dual inhibitor of PI3K/AKT and MAPK/ERK pathways and an excellent therapeutic choice for improved outcomes of PAC patients.

* Corresponding author at: Amity Institute of Molecular Medicine & Stem Cell Research, Amity University, Sector 125, Noida, Uttar Pradesh, 201303, India.
** Corresponding author at: Department of Microbiology, University of Kalyani, Kalyani, Nadia, West Bengal 741235, India.
*** Corresponding author at: Department of Chemistry, Acharya Prafulla Chandra College, New Barrackpore, Kolkata, 700131, India.
E-mail addresses: aroy2@amity.edu (A. Roy), sandipsaha2000@yahoo.com (S. Saha), supratimmicro19@klyuniv.ac.in (S. Mandal).
[1] Equal contribution.

https://doi.org/10.1016/j.molstruc.2026.145636
Received 14 November 2025; Received in revised form 28 January 2026; Accepted 9 February 2026
Available online 11 February 2026

1. Introduction

Prostate adenocarcinoma (PAC) is the second most common male malignancy and each year, more than 600,000 men are estimated to die from this pathology worldwide [1]. Although patients with PAC initially respond to androgen deprivation therapy (ADT) which utilizes orchiectomy or chemical castration using antiandrogens like enzalutamide, eventually individuals develop therapy resistant, metastatic, castration-resistant prostate cancer (mCRPC) which has poor prognosis and high mortality rate [2]. mCRPC development is a complicated and multifactorial process that requires the activation of several signalling pathways, changes in the androgen receptor (AR) signalling, acquirement of genomic and epigenetic changes, activation of non-AR signalling pathways such as PI3K/AKT/mTOR and Wnt/-catenin pathways [3]. Furthermore, emerging evidence suggests that the tumour microenvironment (TME) , specifically the communication between cancer and stromal cells plays a major role in the development of mCRPC [4]. Moreover, a significant fraction of patients with mCRPC eventually develops neuroendocrine prostate cancer (NEPC), which is an aggressive and chemo-resistant subtype of PAC characterized by expression of several neuroendocrine markers including synaptophysin (SYP), neuron-specific enolase (NSE) and chromogranin A (CgA) [5,6]. Apart from ADT, many other therapeutic approaches including immunotherapy and targeted alpha therapy (TAT) have been developed to better manage PAC [7]. Additionally, Ac^{225}-conjugated PSMA (prostate-specific membrane antigen) and Lutetium-177 (Lu^{177}) labelled antibodies showed promise against mCRPC [8,9]. Nonetheless, several challenges including cross-resistance between drugs, limitations in precise targeting of splice variants of androgen receptor (AR) and devising methods to inhibit ligand-independent activation of AR signalling severely hampered improved management of patients with mCRPC. Hence, design, synthesis and development of novel therapeutic interventions and identification of their targets in this deadly pathology is highly warranted [10].

In coordination chemistry, Schiff base is a major class of ligand synthesized from condensation of ketones or aldehydes (carbonyl compounds) with primary amine [11,12]. Schiff base transition metal complexes are synthesized when the ligand Schiff base coordinates with metal ions via azomethine (-C=N) nitrogen and several reports suggest that azomethine linkage is essential for many biological properties conferred by the metal complex including anti-cancer activity [13–15]. Depending on their structural diversity, several Schiff base metal complexes are synthesized which significantly contribute to many aspects of chemical and biological applications including targeted therapy, precision medicine and drug delivery [16–19]. For design and synthesis of Schiff base metal coordination polymer and metal-organic frameworks, several pseudohalides like N_3^-, SCN^-, and $[N(CN)_2]^-$ are used as linkers, among which azido anion is of great interest [20]. It can form both covalent and ionic bonds with metal ions and recent reports suggest that a variety of azido Schiff base metal complexes with discrete or one, two, and three-dimensional structures can be synthesized which can be used as successful therapeutic interventions in biomedical research [21–23]. Among transition metals, zinc is essential and one of the most abundant elements which is critical for several cellular and physiological functions [24]. It plays critical roles in defining structural, regulatory and catalytic properties of many proteins among which zinc fingers are most abundant class of metalloproteins [25,26]. Due to small size and filled (n-1) d -shell, zinc ions display higher ion-dipole contribution, improved polarization or deformation to bond with ligands in the process of complex synthesis. Moreover, zinc can adopt a flexible coordination in its environment, and its geometry can change from tetrahedral to octahedral structure. Therefore, several research groups have reported di and tri-nuclear Zn (II) complexes using different types of Schiff base ligands and assessed their biological functions in respect to human health and disease [17,27,28]. Importantly, normal prostate cells and PAC tumor cells show distinct affinity towards zinc for their metabolic functioning. As compared to normal prostatic glandular epithelial cells, PAC cells rely on very low zinc levels to activate citrate oxidation process, thereby becoming more energy efficient through the completion of the Krebs cycle to produce coupled energy and hence, increasing the level of circulating zinc via administering zinc (II) Schiff base complexes could be an efficient approach for modulating zinc metabolism pathway in PAC cells and promoting suppression of tumor growth [29].

In this research, we report synthesis of a novel azido trinuclear zinc (II) Schiff base complex[$\{ZnL(N_3)\}_2$ Zn]. H_2O (1) (termed compound AR1 or 'ComAR1') and its characterization, crystal structure and spectral studies. Biological evaluation of ComAR1 revealed that it significantly suppressed PAC cell proliferation, EMT, migration and induced G0/G1 cell cycle arrest followed by membrane leakage, chromatin condensation, cell death and apoptosis. Molecular docking analysis revealed that ComAR1 displayed favourable interaction with components of several signalling circuits associated with tumorigenesis including Raf1, TGFβ1 and JAK2. Mechanistically, ComAR1 dampened activation of PI3K/AKT and Ras/MAPK/ERK1/2 pathways in PAC cells, which are critical for tumor cell survival and proliferation. Moreover, ADMET analysis of ComAR1 revealed excellent pharmacokinetic profiles and drug-likeness features including non-hepatotoxicity, non-permeability to blood-brain barrier (BBB), improved bioavailability and reduced potential for drug-drug interaction. Taken together, our results suggest that ComAR1 is an excellent drug candidate for PAC which might emerge as a novel dual inhibitor of PI3K/AKT and MAP kinase signalling in cancer.

2. Materials and methods

2.1. Synthesis of Schiff base ligand (H_2L) and [$\{ZnL(N_3)\}_2$ Zn]. H_2O (ComAR1)

All the chemicals and regents including methanol (Sigma, Cat# 34860), 1,4-butadiene (Sigma, Cat# 509140), 3-methoxy salicylaldehyde (Sigma, Cat# 434086), Zn (II) acetate (Sigma, cat# 383317), and sodium azide (Sigma Cat# S2002), gefitinib (Sigma, Cat# SML1657) and propidium iodide (Thermo, Cat# P1304MP) were >95% pure as analyzed by HPLC. For the synthesis of Schiff base ligand (H_2L), 1 mmol of 1,4- butadiene was dissolved in 10 ml of methanol and 2 mmol solution of 3-methoxy salicylaldehyde was dropwise added to the methanolic solution with stirring followed by reflux at 100^0 C for 2 hours. To synthesize ComAR1, 1.5 mmol of Zn (II) acetate was dissolved in 10 ml of methanol and the solution was added dropwise to Schiff base ligand (H_2L) followed by reflux for 2 hours. Next, the mixture was cooled down to room temperature and 2 ml aqueous solution of 2 mmol of NaN_3 was added to this mixture followed by reflux for 1 hour. The resulting solution was slowly evaporated for 1 week and yellow crystalline product of ComAR1 was obtained. The stability of ComAR1 was assessed by dissolving it in 1X PBS at a concentration of 1 μg/ml followed by incubation at 37 °C for different times (0-48 hr) and absorbance spectrum scanning using UV-Visible spectrophotometer.

2.2. Determination of X-ray crystal structure of ComAR1 and its Hirshfield surface analysis

A yellow, single crystal of ComAR1 was analyzed using X-Ray diffraction method. The crystallography data of ComAR1 was collected at 293 K on Bruker APEXII diffractometer using graphite monochromatic M_0 -K_α radiation at λ=0.71073A^0. The APEXII program was used to collect frame data, lattice parameters, and reflection index of ComAR1 crystal. The crystal structure of ComAR1 was solved by direct methods using SHELXT and cell refinement was performed using full-matrix least-squares on F^2 using SAINT. Nonhydrogen atoms were refined using anisotropic thermal parameter. All hydrogen atoms were placed in their geometrically idealized position in the crystal structure. The lattice water molecule is disordered over two orientations about a

centre of symmetry, and the two components of disorder were refined with a fixed occupancy of 0.25. The CCDC ID of ComAR1 is 2355889. The Hirshfield surface (HS) analysis of ComAR1 crystal was performed using CrystalExplorer tool [30]. Briefly, the electron densities obtained from tabulations of atomic wavefunctions expanded using exponential-type basis functions were explored and several HS surfaces including d_e (Distance from HS to the nearest atom E external to the surface), d_i (Distance from HS to the nearest atom I internal to the surface), d_{norm} (Normalized sum of d_e and d_i), fragment patch (Unique (coloured) region based on atoms external to the HS designed to indicate the nearest-neighbouring molecule), curvedness (function depending on the HS concavity or convexity), shape index (function depending on the HS flatness or curvature) and electron density were obtained. Quantum-mechanical properties were calculated using B3LYP/6-31G(*d, p*) wavefunctions.

2.3. Cell culture, cell proliferation and clonogenic assay

Prostate adenocarcinoma (PAC) cell lines DU145 was obtained from National Centre for Cell Sciences (NCCS), India. PC3 cell was a kind gift from Prof. Simran Tandon, Amity Institute of Molecular Medicine & Stem Cell Research, Amity University Noida (STR profiles of DU145 was added as supplementary Fig. S1). DU145 and PC3 cells were cultured in DMEM and Ham's F12 medium, respectively, supplemented with 10% foetal bovine serum (FBS), 1x penicillin/streptomycin at 37°C in a humidified atmosphere incubator containing 5% CO_2. Cells were routinely tested for mycoplasma contamination using MycoAlert Plus Mycoplasma detection kit (Lonza). Cells were seeded at a density of 7000 cell/well in 96 well plate, treated with different doses of ComAR1 for 72 hours and MTT assay was performed to evaluate cell viability. The experiments were conducted in triplicates, and the results were represented as mean ± SD. For clonogenic assay, DU145 and PC3 cells were seeded at 500/well in 6-well plates, treated with respective IC_{50} values of ComAR1 (obtained from MTT assay) for 14 days. Thereafter, the cells were fixed with 100% methanol, stained with 0.25% crystal violet and the colonies were counted.

2.4. Fluorescence microscopy and cell cycle analysis

Cells treated with control (DMSO) or ComAR1 were grown on poly-L-lysine coated coverslips, washed with 1X PBS and fixed in 4% paraformaldehyde for 30 minutes at room temperature. The fixed cells were washed twice with 1X PBS and incubated with 100 µg/ml propidium iodide (PI) for 30 mins. The images were analyzed using Leica fluorescence microscope fitted with 63X objective. For cell cycle analysis, flow cytometry was performed as described previously [31]. Briefly, trypsinized cells were collected, washed with ice cold 1X PBS, resuspended in ice cold 70% ethanol and fixed overnight by incubating at 4°C. The fixed cells were washed twice with 1X PBS and incubated with 100 µg/ml propidium iodide (PI) and 1 mg/ml RNase A dissolved in FACS buffer (0.1% glucose in 1X PBS) for 30 mins. Cells were analyzed by BD Accuri (BD Biosciences) flow cytometer, and the results were analyzed in BD Accuri C6 software. A total of 10,000 events were counted.

2.5. Apoptosis assay

Trypsinized cells were washed twice with ice-cold 1X PBS and stained with Annexin V-Alexa fluor 488 antibody and propidium iodide (Molecular Probes, Thermo Fisher Scientific, USA) according to manufacturer's protocol. Cells were analyzed by BD Accuri (BD Biosciences) flow cytometer, and the results were analyzed in BD Accuri C6 software.

2.6. Wound healing and cell migration assay

For wound healing assay, 1×10^6 cells were seeded in 24-well plates and incubated at humidified incubator containing 5% CO_2 at 37 °C for 16-22 hours till they reached ~70% confluency. The monolayers were gently scratched using a sterile 10µl pipette tip and carefully washed with medium to remove the detached cells. The cultures were treated with DMSO (control) or ComAR1 for 16 hours and photographed using Eclipse inverted microscope (Nikon). Cell migration was analyzed by Biocoat Matrigel migration assay (Corning, USA) as per manufacturer's protocol. Briefly, 5×10^4 cells were resuspended in DMEM medium containing 0.1% FBS and seeded in the upper chamber. The lower chamber contained chemoattractant medium (DMEM medium supplemented with 15% FBS). After incubating the cells for 16 hours at humidified incubator containing 5% CO_2 at 37 °C, the cells were fixed by 100% methanol, stained by 0.25% crystal violet and the images were analyzed using Eclipse inverted microscope (Nikon).

2.7. RNA isolation and qRT-PCR

Total RNA was extracted using Trizol reagent from the PAC cells treated with DMSO (vehicle control) or ComAR1. Reverse transcription of 2 µg of total RNA was performed using iScript cDNA synthesis kit (Bio-Rad) according to manufacturer's instructions. qRT-PCR analysis was performed using iTaq SYBR Green Supermix (Bio- Rad, USA) using Step One Plus qRT-PCR thermal cycler (Applied Biosystems). PCR consisted of a 15-minute 95°C denaturation step followed by 45 cycles of 15 seconds at 94°C, 20 seconds at 62°C, and 20 seconds at 72°C. Normalized values for specific gene expression were calculated using $2^{-\Delta\Delta Ct}$. β-actin was used as a housekeeping gene and to normalize the expression of target genes. The experiments were performed in triplicates, and the results were plotted using Graph Pad Prism software. The sequences of primers used in the experiments are listed in supplementary table S1B (Supplementary Table ST1).

2.8. Molecular docking

To identify optimal targets for our compound, a set of plausible protein targets were retrieved from the RCSB Protein Data Bank (https://rcsb.org/). Binding sites were detected using CaverWeb 2.0 (https://loschmidt.chemi.muni.cz/caverweb/) [32], and proteins lacking defined catalytic pockets were excluded. Each protein was pre-processed using OpenMM's PDB Fixer tool for structure cleaning, followed by Reduce to add missing hydrogens. The The Forli Lab's Meeko package was further used to assign partial Gasteiger charges and atom types, and to convert structures to PDBQT format for molecular docking with AutoDock Vina v1.2.0 [33]. Docking configurations (grid coordinates and box size) were based on CaverWeb outputs. The ComAR1 ligand was prepared using the established protocol, though the zinc ion necessitated a manual assignment of a +2 charge, representing its physiological Zn (II) oxidation state essential for correct ligand-receptor electrostatic interactions, to overcome the software's constraints regarding metal parameterization.

2.9. Molecular dynamics simulations and ADMET analysis

The stability of the top five ComAR1–protein complexes were evaluated via 200 ns molecular dynamics (MD) simulations using the Desmond module in Maestro 12.5 (Schrödinger Suite 2020-3). The System Builder tool was used to create each solvated model, embedding the complex in an orthorhombic water box with a 10 Å buffer distance on all sides, using the SPC water model. The OPLS3e force field was selected for all atoms. Each system was neutralized by randomly adding appropriate counterions (Na^+ or Cl^-), and physiological ionic strength was maintained by adding 0.15 M NaCl. Energy minimization was performed using default settings to relieve any steric clashes or bad contacts. Subsequently, the systems were equilibrated under the NPT ensemble (constant Number of particles, Pressure, and Temperature). A temperature of 300 K and pressure of 1 atm. were maintained using the Nose–Hoover thermostat and the Martyna–Tobias–Klein barostat,

respectively. RESPA integrators were used for time integration, with a 2-fs time step for bonded and near non-bonded interactions, and 6-fs for far non-bonded interactions. Production MD simulations were carried out for 200 ns, saving 1000 frames per trajectory (~1 frame every 200 ps) for analysis. Simulation trajectories were analyzed using the Simulation Interaction Diagram (SID) tool in Desmond to evaluate key parameters such as root mean square deviation (RMSD), root mean square fluctuation (RMSF), protein–ligand contacts, hydrogen bonding, and ligand stability within the binding site. The pharmacokinetic properties of the synthesized compounds were investigated using the online software program SWISS ADME. The outputs from these programs can be further interpreted considering established guidelines such as Veber's rule and Lipinski's rule of five, which are critical for predicting the oral bioavailability of drug candidates. The chemical properties of the compounds were thoroughly evaluated through the SWISS ADME program, which provided insights into their structural characteristics.

2.10. Western blotting and densitometric analysis

Western blotting was performed as described earlier [34]. Briefly, DMSO or ComAR1-treated PAC cells were lysed in RIPA lysis buffer (50 mM Tris, pH 7.4, 150 mM NaCl, 1% Triton X-100, 1% sodium deoxycholate, 0.1% sodium dodecyl sulfate, protease/phosphatase inhibitor cocktail). 25 μg of proteins were resolved in 10% SDS-PAGE and transferred to PVDF membranes. The blots were blocked in blocking buffer (5% non-fat milk suspended in 1X PBS+0.1% Tween 20, pH 7.6) for 1 hour at room temperature and incubated with primary antibodies [anti-Bcl-2 (rabbit monoclonal, CST, Cat# 3498T), anti-Bax (rabbit polyclonal, CST, Cat# 2772T), anti-AKT (rabbit polyclonal, Affinity, Cat# AF6261), anti-phospho-AKT^{Ser473} (rabbit polyclonal, Affinity, Cat# AF0016), anti-PI3K (rabbit polyclonal, Affinity, cat# AF6241), anti-phospho-PI3K^{Tyr607} (rabbit polyclonal, Affinity, cat# AF3241), anti-ERK1/2 (rabbit polyclonal, Affinity, cat# AF0155), anti--phospho-ERK1/2$^{Thr202/Tyr204}$ (rabbit polyclonal, Affinity, cat# AF1015), anti-BAD (rabbit monoclonal, CST, cat# 9292T), anti--phospho-BAD^{Ser112} (rabbit monoclonal, CST, cat# 9291T), anti--phospho-BAD^{Ser136} (rabbit monoclonal, CST, cat# 9295T), anti-p21-RAS (rabbit monoclonal, CST Cat# 3965T) and anti-Actin (rabbit monoclonal, CST, Cat# 4967)] diluted in blocking buffer at a ratio of 1:1000 overnight at 4°C, followed by incubation with secondary antibody conjugated with horseradish peroxidase (HRP) (anti-rabbit IgG-HRP, CST, cat# 7074) diluted in blocking buffer at a ratio of 1:10000 for 2 hours at room temperature. The blots were incubated with ECL chemiluminescence substrate (Pierce, USA) for 2 mins at room temperature under dark condition and further developed using X-ray films (Fujifilm) in dark room. Briefly, X-ray developer and fixer powders (Apex Digital) were separately dissolved in 9 litre of double distilled water as per manufacturer's protocol. X-ray films were exposed to immunoblots inside an X-ray cassette followed by development and fixation. Western blotting was performed in three biological replicates (supplementary Fig.s S2-S7) and representative images were reported. Densitometric analysis of immunoblots was performed as previously described [35]. Briefly, ImageJ software (NIH) was used to convert the immunoblot images into greyscale and brightness/contrast adjustment was done followed by background subtraction. The Gel Analyzer tool of ImageJ was used to determine the profiles of the bands. The values of the target proteins were normalized against the band intensities of Actin, and the results were plotted using Graph Pad Prism software.

2.11. Statistical analysis

Data analysis was done using the student *t* test for comparison between two groups (two-tailed). All statistical analyses were performed using Graph Pad Prism IX software. All values are represented as mean ± SD of at least three independent experiments. A p value < 0.05 was considered significant (*, $p < 0.05$; **, $p < 0.01$; *** $p < 0.001$; #, $p < 0.0001$; ns, not significant).

3. Results

3.1. Synthesis, spectral characterization and X-ray diffraction analysis of tetradented H_2L Schiff base ligand and its complex (ComAR1)

The tetradented H_2L Schiff base ligand was synthesized by refluxing 1,4-butadiamine and 3-methoxysalicyaldehyde in a 1:2 mmol ratio in methanolic solvent, purified and processed further to synthesize ComAR1. Reflux of zinc acetate dihydrate with H_2L ligand in methanol followed by slow addition of aqueous solution NaN_3 in a molar ratio of 1:1.5:1 resulted in synthesis of ComAR1 harbouring a pentadentate ligand (Fig. 1A). The crystal of ComAR1 (Fig. 1B) was yellow in colour, air-stable and soluble in common organic solvents including DMSO. IR spectrometry results showed that ComAR1 produced sharp peak at 1632, 2065 and 2954 cm^{-1} due to the presence of azomethane group (-C=N), azido anion ($N_3^{-1)}$ and –OH group of water molecule, respectively (Fig. 1C). The UV-visible spectral analysis of DMSO-solubilized ComAR1 displayed absorption peaks of 233, 274, and 361 nm due to ligand-to-metal charge transfer (LMCT), π-π*, and n–π* transitions, respectively (Fig. 1D, left panel). The analytical formula of ComAR1 was $C_{40}H_{44}N_{10}O_8Zn_3$, 0.5 ($H_2O$) with atom constituents of C (48.14%), H (4.54%), N (14.03%), O (13.62%) and Zn (19.65%).

Next, we sought to analyze the properties of crystalline ComAR1 using X-ray diffraction method (Fig. 1B) [36]. ComAR1 crystallized in monoclinic space group P 21/'n and the symmetry unit consisted of 3 Zn centres, 2 deprotonated Schiff base ligands (L^{2-}) and 2 terminal N_3^- ions. Three Zn centres were Zn1, Zn2, and Zn3, where Zn1 and Zn3 were in terminal positions and Zn2 was in a centre position of ComAR1. Each of the two asymmetric units in ComAR1 consisted of one Zinc (II) metal ion, one Schiff base in fully deprotonating L^{-2} form and one azido ion. The coordination number of Zn1 terminal atom was penta-coordinate with distorted trigonal bipyramidal geometry. The equatorial plane around Zn1 was formed by two nitrogen atoms of an imine nitrogen atom N_2, a nitrogen atom of the azido group N_3, and an oxygen atom of phenoxide with bond distances of 2.120**Å**, 1.987**Å**, and 2.102**Å,** respectively. Similarly, the equatorial plane around Zn3 displayed two nitrogen atoms of an imine nitrogen atom N_7, a nitrogen atom of the azido group N_8, and an oxygen atom of phenoxide with bond distances of 2.045**Å**, 1.996**Å**, and 2.021**Å,** respectively. The additional τ (tau) parameter ($\tau = |b\text{-}a|/60^0$ where 'b' and 'a' are the two largest angles around the central atom) was found to be 0.701 for Zn1 centre. As ideal values of τ (tau) for square pyramidal and trigonal pyramidal structures are 0.0 and 1.0, respectively [37], the Zn1 centre had a distorted trigonal pyramidal structure. The central Zn2 was hexa-coordinated and adopted an octahedral geometry. The equatorial plane of Zn2 was occupied by three phenolic oxygens (O1, O2, and O6) and one methoxy oxygen (O7). The axial position was occupied by one methoxy oxygen (O3) and one phenolic oxygen (O5). The Zn_2-$O_{phenolate}$ bond lengths were in the range of ~1.999-2.029 Å, like Zn^{+2} (central Zn ion) and the Zn_2-O_{ethoxy} bond length was observed to be ~2.305-2.338Å, which was significantly larger than that of Zn_2-$O_{phenolate}$ bond length. The imino (Zn-N_{imino}) and azido (Zn-N_{azido}) nitrogen atoms were found to be coordinated with each Zn (II) ions having bond lengths of 2.045-2.116 and 1.996 Å, respectively. Two Zn (II) clusters Zn1-Zn2 and Zn3-Zn2 were separated by 3.169 and 3.173 Å, respectively. It is well known that H-bonding interactions, namely (O–H…N) regulates packaging of molecules in a crystal [38,39]. In crystal structure of ComAR1, the hydrogen atom H1WB of half-occupied water molecule showed a similar bonding interaction with the non-coordinated terminal nitrogen atom (5A) with a donor-acceptor distance of 2.129 Å. Moreover, both the half-occupied water molecules were hydrogen bonded with each other. Two similar crystals of trinuclear Zn (II) based structure have been previously reported by our group [17,19]. ComAR1 contains a single water molecule just like the earlier reported crystal structures. Furthermore, the bond

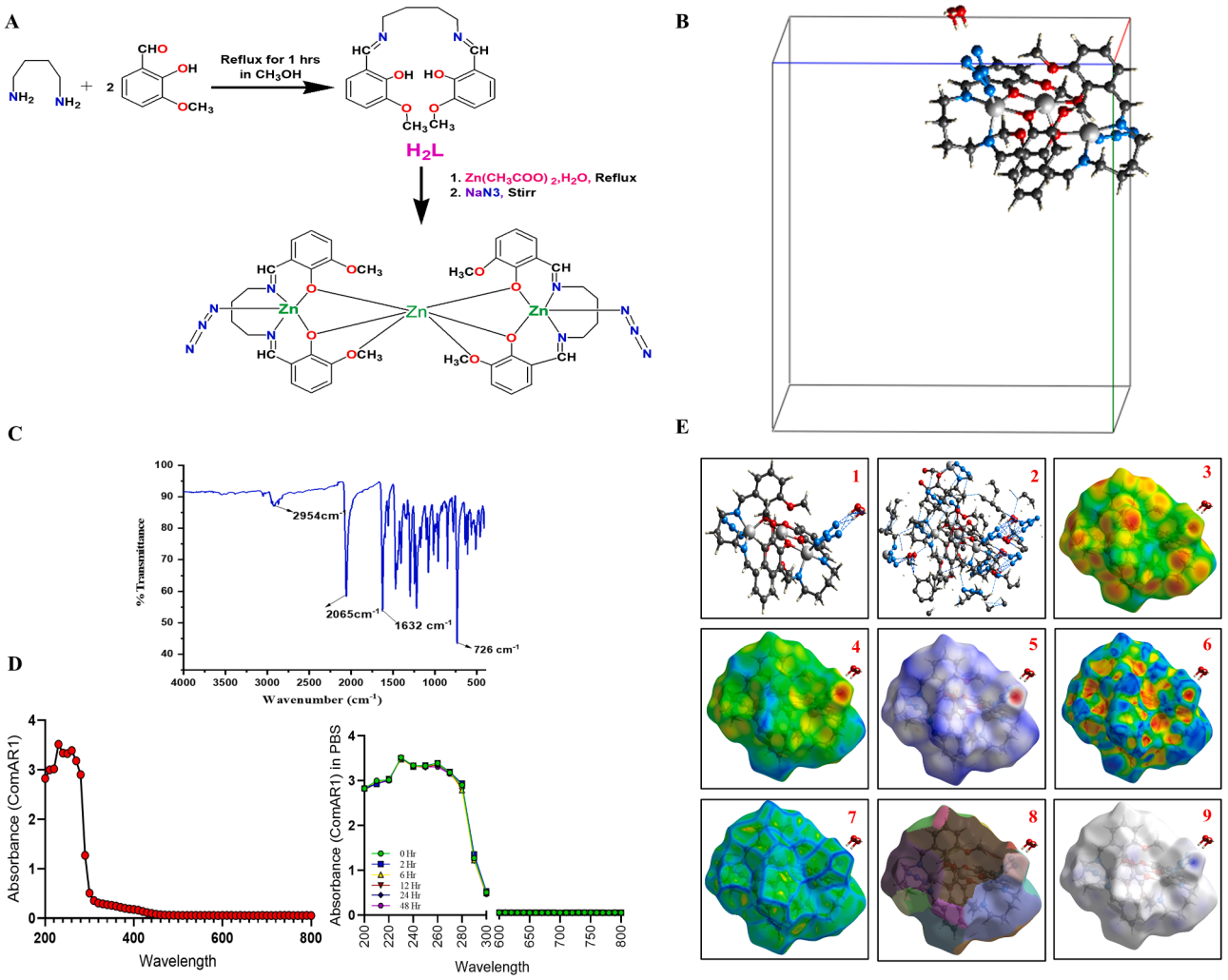

Fig. 1. Synthesis, molecular characterization and Hirshfield surface analysis of ComAR1. A. Schematics of the synthesis route of ComAR1 is shown. **B**. Crystal structure and atomic arrangements of ComAR1 is shown. **C**. FTIR spectroscopic analysis of ComAR1 is represented by spectral graphs. **D.** UV-Visible spectroscopic analysis of ComAR1 is shown by spectral graph (left panel). ComAR1 was dissolved in 1X PBS at a concentration of 1 μg/ml, incubated at 37 °C for indicated times and subjected to UV-Visible spectroscopic analysis (right panel). **E.** Intermolecular hydrogen bonds between ComAR1 and H_2O molecule (inset 1) and atoms within a radius of 4 Å and several Hirshfield surface analyses (d_i, d_e, d_{norm}, shape index, curvedness, fragment patch and electron density in insets 2-9, respectively) were analyzed using CrystalExplorer tool.

distances and angles observed in this complex are almost identical to the crystals reported in those previous studies. Crystal parameters, selected refinement details for ComAR1 and bond parameters along with bond angles are given in Tables 1 and 2. The empirical formula of ComAR1 to be $C_{40}H_{44}N_{10}O_8Zn_3$, 0.5 ($H_2O$); with atomic composition of: C (48.14%), H (4.54%), N (14.03%), O (13.62%) and Zn (19.65%). Furthermore, FTIR (KBr cm^{-1}) and UV-Vis spectroscopic studies identified signature peaks of: ν: (-C=N) 1632 cm^{-1}, (ν_{N3})2065 cm^{-1} and (ν_{OH}) 2954 cm^{-1}, λ_{max} (nm) (ε, M^{-} cm^{-}) 233 nm (270700), 274 nm (65130) and 361 nm (23324) (Fig. 1C). The stability of ComAR1 was assessed using UV-Visible spectroscopy. It was dissolved in 1X PBS at a concentration of 1 μg/ml, incubated at 37 °C for different time points (0-48 hr) followed by absorption spectrum scanning. Our results showed that ComAR1 displayed highly similar absorption spectra with λ_{max} at 233 nm with no additional peaks even at 48 hours-displaying its superior stability under physiological conditions (Fig. 1D, right panel). Finally, we analyzed intermolecular interactions and several Hirshfield surface (HS) properties of ComAR1 using Crystal Explorer tool [30]. ComAR1 exhibited intermolecular hydrogen bonds with the water molecule (blue dashed line, Fig. 1E, inset 1) and atoms within the radius of 4 Å (blue dashed line, Fig. 1E, inset 2). Quantum-mechanical properties were calculated using B3LYP/6-31G(*d,p*) wavefunctions and HSs including d_e (Distance from HS to the nearest atom E external to the surface), d_i (Distance from HS to the nearest atom I internal to the surface), d_{norm} (Normalized sum of d_e and d_i), fragment patch (Unique (coloured) region based on atoms external to the HS designed to indicate the nearest-neighbouring molecule), curvedness (function depending on the HS concavity or convexity), shape index (function depending on the HS flatness or curvature) and electron density (Fig. 1E, insets 3-9) were obtained.

3.2. *ComAR1 suppresses proliferation and induces plasma membrane leakage in PAC cells*

First, to examine any cytotoxic potential of ComAR1 on PAC cells, we treated PNT2 (SV40-immortalized normal prostate epithelial cell), PAC cells DU145 and PC3 with different concentrations of the compound and analyzed its effect by MTT assay. It was revealed that ComAR1 suppressed PAC cell proliferation in a dose-dependent manner with significantly lesser effect on PNT2 cells (Fig. 2A). IC_{50} values of ComAR1 for PNT2, DU145 and PC3 were 433 ± 28, 100 ± 13 and 65 ± 8 μg/ml, respectively (Fig. 2B). These results suggest that ComAR1 has minimal cytotoxic effect on normal prostate epithelial cells, and it selectively

Table 1
Crystal parameters and selected refinement details for ComAR1.

Empirical formula	C40 H45 N10 O8.50 Zn3′
Formula weight	997.97
Temperature/K	293(2)
Crystal system	Monoclinic
Space group	P 21/n'
a/Å	9.3695(6).
b/Å	22.4236(13)
c/Å	20.2964(12)
α/°	90
β/°	95.417(2)
γ/°	90
Volume/Å^3	4245.2(4)
Z	4
ρ_{calc}g/cm^3	1.561
μ/mm^{-1}	1.747
F (000)	2052
Radiation	MoK\a (0.71073)
2Θ range for data collection/°	1.816-25.500
Index ranges	-11 ≤ h ≤ 11, -27 ≤ k ≤ 27, -24≤ l ≤ 24
Reflections collected	109149
Independent reflections	7907 [R_{int} = 0.0584, R_{sigma} = 0.1297]
No. of reflections with *I* > 2σ(I)	5546
Data/restraints/parameters	7907/13/573
Goodness-of-fit on F^2	1.064
Final R indexes [I≥2σ (I)] [a,b]	R1 =0.0482, wR2 = 0.1072
Final R indexes [all data]	R_1 =0.0851, wR_2 =0.1295

Table 2
Bond distances (Å) and angles (°) around the metal centres in ComAR1.

Atoms	**Distance**	**Atoms**	**Distance**	**Atoms**	**Distance**
Zn1-O1	2.010(3)	Zn2– O2	2.002(3)	Zn3– N8	1.996(5)
Zn1- O2	2.102(3)	Zn2 -O3	2.305(3)	Zn3– O5	2.021(3)
Zn1-N1	2.120(4)	Zn2- O5	2.002(3)	Zn3 –O6	2.027(3)
Zn1- N2	2.043(4)	Zn2- O6	2.027(3)	Zn3 – N6	2.116(4)
Zn1- N3	1.987(5)	Zn2- O7	2.338(2)	Zn3 – N7	2.045(4)
Zn2- O1	1.999(3)				
Atoms	**Angle**	**Atoms**	**Angle**	**Atoms**	**Angle**
O1-Zn1-O2	76.4	O1-Zn2-O3	74.0(1)	O5-Zn2-O6	78.3(1)
O1-Zn1-N1	87.4(1)	O1-Zn2-O5	156.7(1)	O5-Zn2-O7	72.6(1)
O1-Zn1-N2	117.0(1)	O1-Zn2-O6	120.0(1)	O6-Zn2-O7	150.8(1)
O1-Zn1-N3	120.8(2)	O1-Zn2-O7	87.8(1)	O5-Zn3-O6	76.3(1)
O2-Zn1-N1	162.9(1)	O2-Zn2-O3	152.3(1)	O5-Zn3-N6	88.0(1)
O2-Zn1-N2	87.1(1)	O2-Zn2-O5	114.8(1)	O5-Zn3-N7	119.5(1)
O2-Zn1-N3	94.3(2)	O2-Zn2-O6	99.8(1)	O5-Zn3-N8	120.9(2)
N1-Zn1-N2	95.8(2)	O2-Zn2-O7	94.1(1)	O6-Zn3-N6	162.5(1)
N1-Zn1-N3	98.6(2)	O3-Zn2-O5	91.5(1)	O6-Zn3-N7	86.4(1)
N2-Zn1-N3	120.7(2)	O3-Zn2-O6	93.7(1)	N6-Zn3-N8	94.5(1)
O1-Zn2-O2	78.3(1)	O3-Zn2-O7	85.3(1)	N6-Zn3-N8	100.3(/2)
				N7-Zn3-N8	117.8(2)

Symmetry element [a]=1/2-X,1/2+Y,1/2-Z

targets PAC cells to impart its anti-proliferative effect. Clonogenic assay further confirmed that ComAR1 significantly suppressed PAC cell proliferation (Fig. 2C). As ComAR1 significantly displayed anti-proliferative potential at a concentration of its calculated IC_{50} values (100 ± 13 and 65 ± 8 μg/ml for DU145 and PC3, respectively), we treated DU145 and PC3 with ComAR1 at a dose of 100 and 65 μg/ml, respectively in further experiments. It is reported that several therapeutics including synthetic compounds disrupt plasma membrane architecture resulting in suppression of cell proliferation and cell death which can be measured by propidium iodide (PI) uptake followed by fluorescence microscopy or flow cytometry [40–42]. We investigated if ComAR1 could induce membrane rupture followed by anti-proliferative effect and cell death in PAC cells. Indeed, it significantly induced plasma membrane leakage, increased permeability to PI intake and cell death in both DU145 and PC3 cells (Fig. 2D). Taken together, our results suggested that ComAR1 significantly suppressed PAC cell proliferation, induced plasma membrane leakage and cell death.

3.3. Suppression of PAC cell EMT, migration and invasion by ComAR1

The propensity of tumor cells to transition from epithelial to mesenchymal phenotype via epithelial–mesenchymal transition (EMT) program can regulate metastatic processes, cancer progression, and treatment resistance [43]. Given that ComAR1 exerted cytotoxic and anti-proliferative potential in DU145 and PC3 cells, we examined if it impacts EMT and metastatic potentials of these PAC cells. As alterations in expression of several transcription factors and markers such as Snail, Twist and a 'cadherin switch' are hallmarks of EMT in tumor cells [43–45], we assessed the expression of E-cadherin, N-cadherin and vimentin in ComAR1-treated PAC cells. DU145 and PC3 cells were treated with 100 and 65 μg/ml of ComAR1 for 16 hours, respectively and expressions of E-cadherin, N-cadherin and vimentin were analyzed by qRT-PCR and Western blotting. It was revealed that ComAR1 significantly suppressed expression of N-cadherin, vimentin and that of E-cadherin was augmented at both mRNA and protein levels (Fig. 3A-C). Wound healing assay was performed to assess the anti-migratory potential of ComAR1 in PAC cells. Our results indicated that ComAR1 significantly inhibited DU145 and PC3 wound closure, cell-cell interaction and migration at a concentration of 100 and 65 μg/ml, respectively for two cells (Supplementary Fig. S8, bottom panel). In line with these observations, we also found that ComAR1 suppressed DU145 and PC3 cell invasiveness as analyzed by Matrigel invasion assay (Fig. 3D). Taken together, our results indicated that ComAR1 significantly inhibited PAC cell EMT, migration and invasion.

3.4. ComAR1 induces G0/G1 cell cycle arrest, nuclear condensation and apoptosis in PAC cells

Given that ComAR1 significantly suppressed PAC cell proliferation, we asked if it modulates cell cycle progression of cancer cells as dysregulated cell cycle and uncontrolled cell divisions are hallmarks of cancer [46]. DU145 and PC3 cells were treated with 100 and 65 μg/ml of ComAR1 for 16 hours respectively, stained with propidium iodide (PI) and subjected to flow cytometry to examine cell cycle progression. We observed that ComAR1 induced G0/G1 cell cycle arrest in both PAC cells (Fig. 4A) as population of sub-G1 stage significantly accumulated for both DU145 and PC3 cells upon drug treatment (Fig. 4B). As it is well reported that prolonged cell cycle arrest at G0/G1 border induces apoptosis in cancer cells [47,48], we questioned if ComAR1 could induce apoptosis in PAC cells. DU145 and PC3 cells were treated with IC_{25} and IC_{50} values of ComAR1 (50 and 100 μg/ml for DU145, 32.5 and 65 μg/ml for PC3, respectively) for 16 hours and whole cell lysates were analyzed by Western blotting to assess expression of two apoptotic markers Bcl-2 (anti-apoptotic) and Bax (pro-apoptotic) [49]. We observed that ComAR1 significantly suppressed expression of Bcl-2 at its IC_{50} value in both DU145 and PC3 cells, whereas expression of Bax was markedly augmented in both cells (Fig. 4C). In line with these observations, as analyzed by qRT-PCR, mRNA expression of *BCL2* and *BAX* were significantly modulated when DU145 and PC3 cells were treated with their respective IC_{50} values of ComAR1 (Fig. 4D). As treating PAC cells with IC_{25} values of ComAR1 did not produce any significant effect, we decided to perform further experiments related to apoptosis using IC_{50} values of the compound. As nuclear condensation followed by DNA fragmentation is a marker of apoptosis [50], we treated DU145 and PC3 cells with 100 and 65 μg/ml of ComAR1 for 16 hours respectively, stained with DAPI and analyzed them under fluorescence microscope. It was evident that ComAR1 significantly induced nuclear condensation in PAC cells as compared to control (DMSO) (Fig. 4E, Supplementary Fig. S8). To further validate our results, we treated PAC cells as mentioned above, stained with Annexin V-Alexa Fluor 488 + PI and analyzed them using flow cytometry. Our results indicated that ComAR1 significantly induced apoptosis at both early and late stages (Fig. 4F-G). Taken together, our results clearly showed that ComAR1 induced G0/G1 cell cycle arrest, nuclear condensation, DNA fragmentation followed by

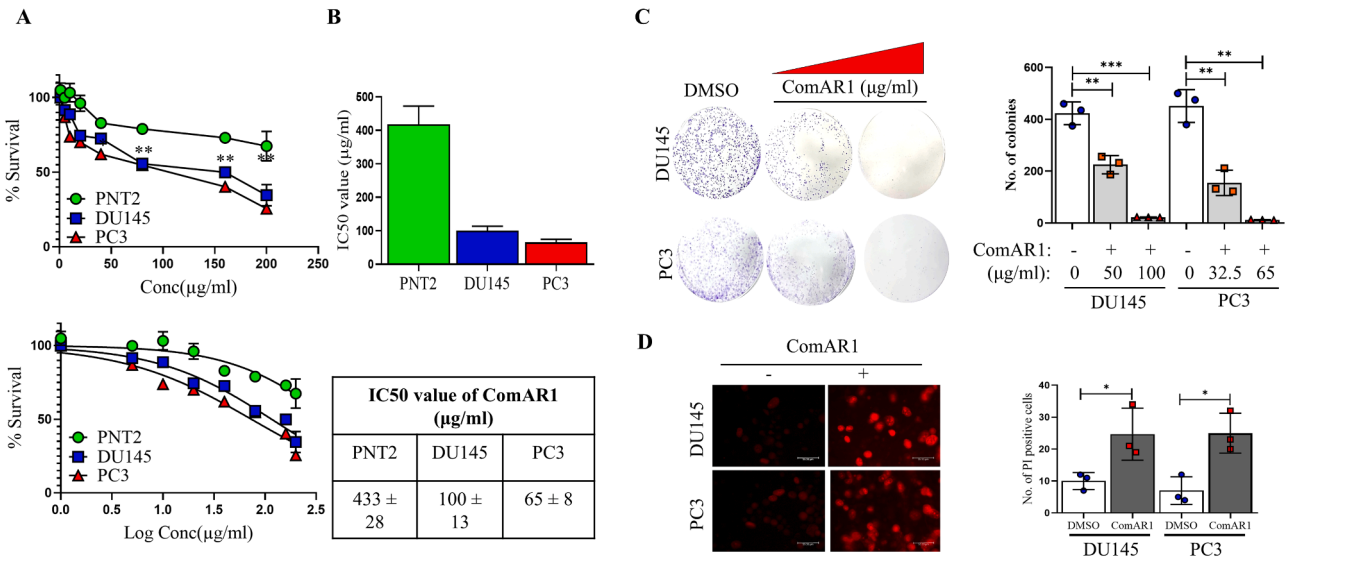

IC50 value of ComAR1 (µg/ml)		
PNT2	DU145	PC3
433 ± 28	100 ± 13	65 ± 8

Fig. 2. ComAR1 suppressed PAC cell proliferation and induces plasma membrane leakage. A. PNT2, DU145 and PC3 cells were treated with different concentrations of ComAR1, and its cytotoxicity was measured by MTT assay. **B**. IC_{50} values (µg/ml) of ComAR1 for three cells were determined after analyzing results from MTT assay and represented graphically. **C**. DU145 and PC3 cells were treated with 100 and 65 µg/ml of ComAR1, respectively and clonogenic assay was performed. **D**. DU145 and PC3 cells were treated with ComAR1 as described in C and plasma membrane leakage was assessed by propidium iodide (PI) staining. All values in the bar graphs were represented as mean ± SD of at least three independent experiments. A p value < 0.05 was considered significant (*, p <0.05; **, p <0.01; *** p <0.001).

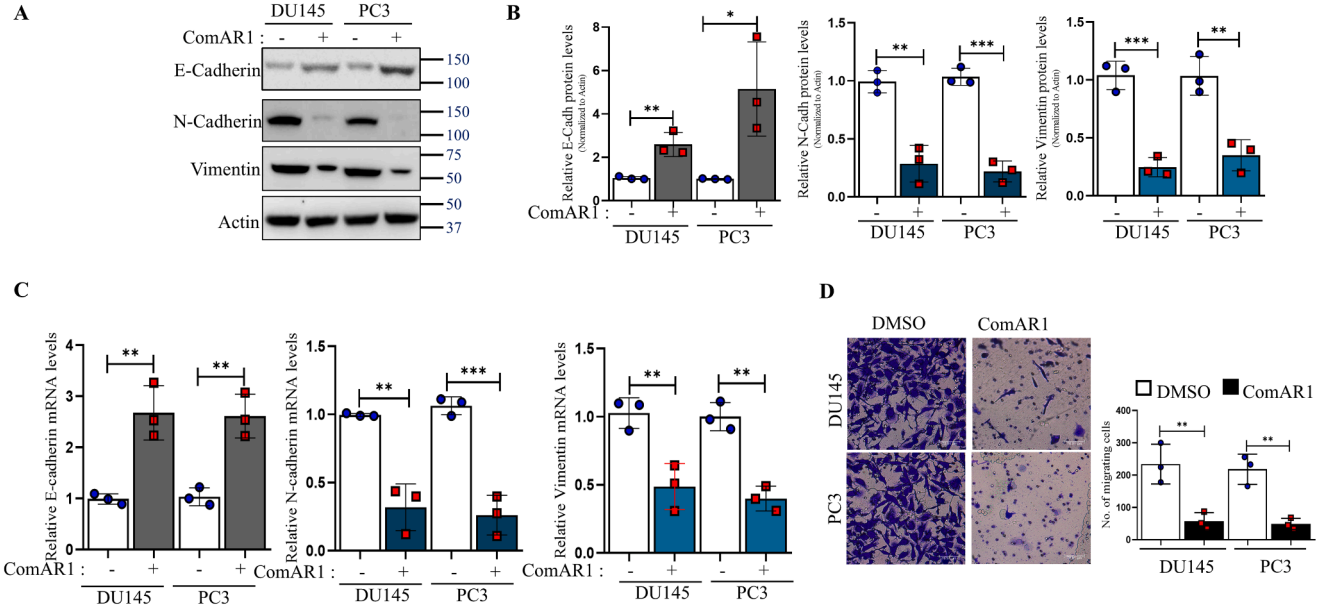

Fig. 3. ComAR1 suppresses PAC cell EMT, migration and invasion. A. DU145 and PC3 cells were treated with 100 and 65 µg/ml of ComAR1, respectively for 16 hours and whole cell lysates were analyzed by Western blotting using designated antibodies. **B**. Densitometric analysis of expressions of E-cadherin, N-cadherin and vimentin in ComAR1-treated PAC cells was performed. **C**. DU145 and PC3 cells were treated with ComAR1 as described in A and mRNA levels of E-cadherin, N-cadherin and vimentin were analysed by qRT-PCR. **D.** DU145 and PC3 cells were treated with ComAR1 as described in A and cell invasion was assessed by Matrigel invasion assay. All values in the bar graphs were represented as mean ± SD of at least three independent experiments. A p value < 0.05 was considered significant (*, p <0.05; **, p <0.01; *** p <0.001). Actin served as loading control in A.

apoptosis in PAC cells DU145 and PC3-indicating its potential as a novel therapeutic choice in PAC.

3.5. Molecular docking and simulation analyses of ComAR1 revealed its interaction with key regulatory proteins involved in carcinogenesis

As our results demonstrated that ComAR1 suppressed proliferation, EMT, migration/invasion and induced plasma membrane leakage, G0/G1 cell cycle arrest, nuclear condensation followed by apoptosis in PAC cells DU145 and PC3, next, we sought to recognize its molecular role and mode of action as a novel treatment option in PAC using *in silico* analyses including molecular docking. This computational technique involves prediction of binding affinity of ligands (ComAR1 herein) to receptor proteins and their interactions at the atomic level [51,52]. Molecular docking is structure-based and requires a high-resolution 3D representation of the target protein obtained through several techniques like

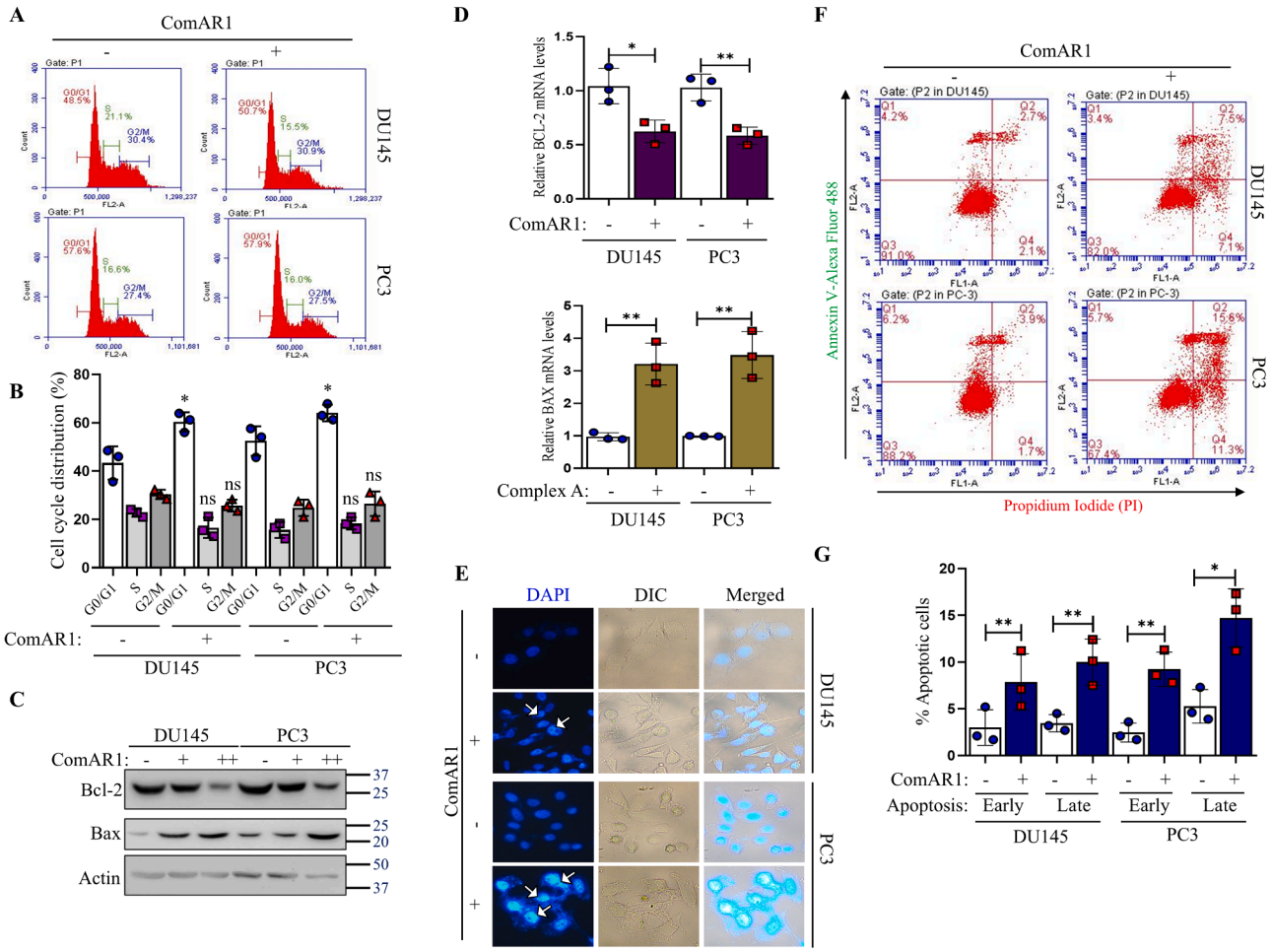

Fig. 4. ComAR1 induces G0/G1 cell cycle arrest and apoptosis in PAC cells. A. DU145 and PC3 cells were treated with ComAR1 as indicated in Fig. 3A, stained with PI and cell cycle analysis was performed by flow cytometry. **B**. Cell cycle distribution of ComAR1-treated PAC cells was represented in bar graph. **C**. DU145 and PC3 cells were treated with ComAR1 (-: DMSO, +: 50 μg/ml, ++: 100 μg/ml for DU145, (-: DMSO, +: 32.5 μg/ml, ++: 65 μg/ml for PC3) for 16 hours and whole cell lysates were analyzed by Western blotting using indicated antibodies. **D**. DU145 and PC3 cells were treated with ComAR1 as indicated in Fig. 3A and mRNA levels of BCL2 and BAX were analyzed by qRT-PCR. **E**. PAC cells treated with ComAR1 as described in Fig. 3A were stained with DAPI and images of nuclear condensation were acquired in fluorescent microscope. **F**. PAC cells treated with ComAR1 as described in Fig. 3A, were stained with Annexin V-Alexa Fluor 488, PI and analyzed for apoptosis in flow cytometer. **G**. Quantification of percentages of early and late apoptotic PAC cells was represented by bar graph. All values in the bar graphs were represented as mean ± SD of at least three independent experiments. A p value < 0.05 was considered significant (*, p <0.05; **, p <0.01; ns, not significant). Actin served as loading control in C.

Table 3
Binding affinities and intermolecular interactions of top 10 substrates of ComAR1.

Protein ID	Protein Name	Binding score (kcal/mol)	Hydrogen bonds	Hydrophobic interactions	π-stacking interactions
3D0E	Akt2	-10.11	THR-162A, GLY-312A	VAL-147B, ASP-151B, LYS-191A, LEU-296A, THR-313A	—
1W98	Cyclin E1	-8.1	ALA-338B	THR-158A, HIS-161A, ILE-190B, PRO-234	—
7LOF	Ras	-8.05	ASP-70A, VAL-103A	LEU-32A, VAL-103A, GLU-108A	—
8V8V	PI3K	-7.91	ASN-170A, GLU-259A, LYS-271A, SER-275A, GLU-849A, LYS-924A	LYS-271A, LEU-279A, LEU-279A, PHE-794A, LEU-834A	—
3CU8	Raf	-7.22	—	ALA-54B, PRO-261Q, ASN-262Q	—
4H39	MAPK	-7.2	ASP-207A	ALA-74A, GLN-75A, ASP-189A, ASP-207A	—
6GJB	Erk2	-7.14	ARG-67A	ALA-35A, THR-190A, ARG-191A	LYS-151A
6SLG	Erk1	-7.04	LYS-151A, SER-153A, ASN-154A	ALA-35A, TYR-113A, THR-190A	LYS-151A
3SL9	β-catenin	-6.86	SER-35A, LYS-131A	VAL-73A, ASN-74A, ALA-77A, LEU-78A, LYS-131A, ALA-153A, TYR-154A	—
8PT3	MAPK1	-6.59	TYR-113A	TYR-113A, LYS-151A, ALA-189A, THR-190A, TRP-192A	—

X-ray crystallography and nuclear magnetic resonance spectroscopy. Moreover, we performed several molecular dynamics simulation studies on ComAR1 including molecular dynamics trajectory analysis for measuring structural stability of ComAR1-substrate complexes.

3.5.1. *Molecular docking analysis of ComAR1*

First, to identify putative ComAR1-interacting substrates, we selected 40 proteins (Supplementary Table T2) which are critical components of several signalling circuits and cellular phenomenon associated with tumorigenesis of the prostate including FOXO [53], JAK/STAT [54] pathways, extracellular matrix remodelling [55] and signalling cascades that control cell cycle and apoptosis [56,57]. Protein entries with unavailable catalytic pocket grid coordinates as determined by Caver Web server were neglected and 20 entries with significant docking scores (kcal/mol) were selected (Supplementary Table T3). Furthermore, top 10 proteins according to their highest binding affinity towards ComAR1 were screened and analyzed for key intermolecular interaction (Table 3). The strongest binding affinity was observed with 3D0E (Akt2, -10.11 kcal/mol), supported by crucial hydrogen bonds with THR-162A and GLY-312A, along with significant hydrophobic contacts with residues like VAL-147B and LEU-296A. Other substrates such as 1W98 (Cyclin E1, -8.10 kcal/mol), 7LOF (Ras, -8.05 kcal/mol), and 8V8V (PI3K, -7.91 kcal/mol), exhibited favourable interactions including multiple hydrogen bonds and hydrophobic contacts which are essential for stabilizing the ligand in the binding pocket. Notably, π-stacking interactions were observed in some ComAR1-substrate complexes including 6GJB (Erk2, -7.14 kcal/mol) and 6SLG (Erk2, -7.04 kcal/mol)-potentially enhancing binding affinity. In contrast, substrates like 8I0M (Cdk6) and 2W96 (Cdk4) showed unfavourable binding with positive docking scores indicating an absence of stable interactions (Supplementary Table T3).

Next, to validate our molecular docking results and to further explore several ligand-substrate interaction parameters including binding pose and molecular dynamics, we identified and included crystal structures of 6GJB (**Erk2**), 6SLG (**Erk2** bound with ERK1/2 inhibitor AZD0364), 8PT3 (**Erk2** covalently bound to RU77 cyclohexanone-based inhibitor), 3D0E (**Akt2** bound with GSK690693), and 7LOF (**HRAS** bound to Monobody 12VC3) for further analysis. The choice for selecting these substrates were three-fold: 1) All of these substrates showed significant binding affinity towards ComAR1 (Table 3), 2) they displayed favourable interactions with ComAR1 including hydrogen bonds and π stacking interactions essential for stabilizing the ligand in the binding pocket and 3) Ras, AKT and ERK2 constitute components of Ras/Raf/MEK/ERK and PI3K/AKT signalling pathways, respectively-whose aberrant activation and function are significantly associated with carcinoma of the prostate [58–60]. Hence, ComAR1 could potentially therapeutically target these axes for improved outcome of the disease. Next, we analyzed several public databases including TCGA to corroborate clinical significance of selected proteins in PAC. Our results showed that *PIK3CA* (encodes for the catalytic subunit of PI3K), *AKT1, HRAS, KRAS, MAPK3* (encodes for Erk1) and *MAPK1* (encodes for Erk2)-components genes of Ras/Raf/MEK/ERK and PI3K/AKT signalling circuits contained

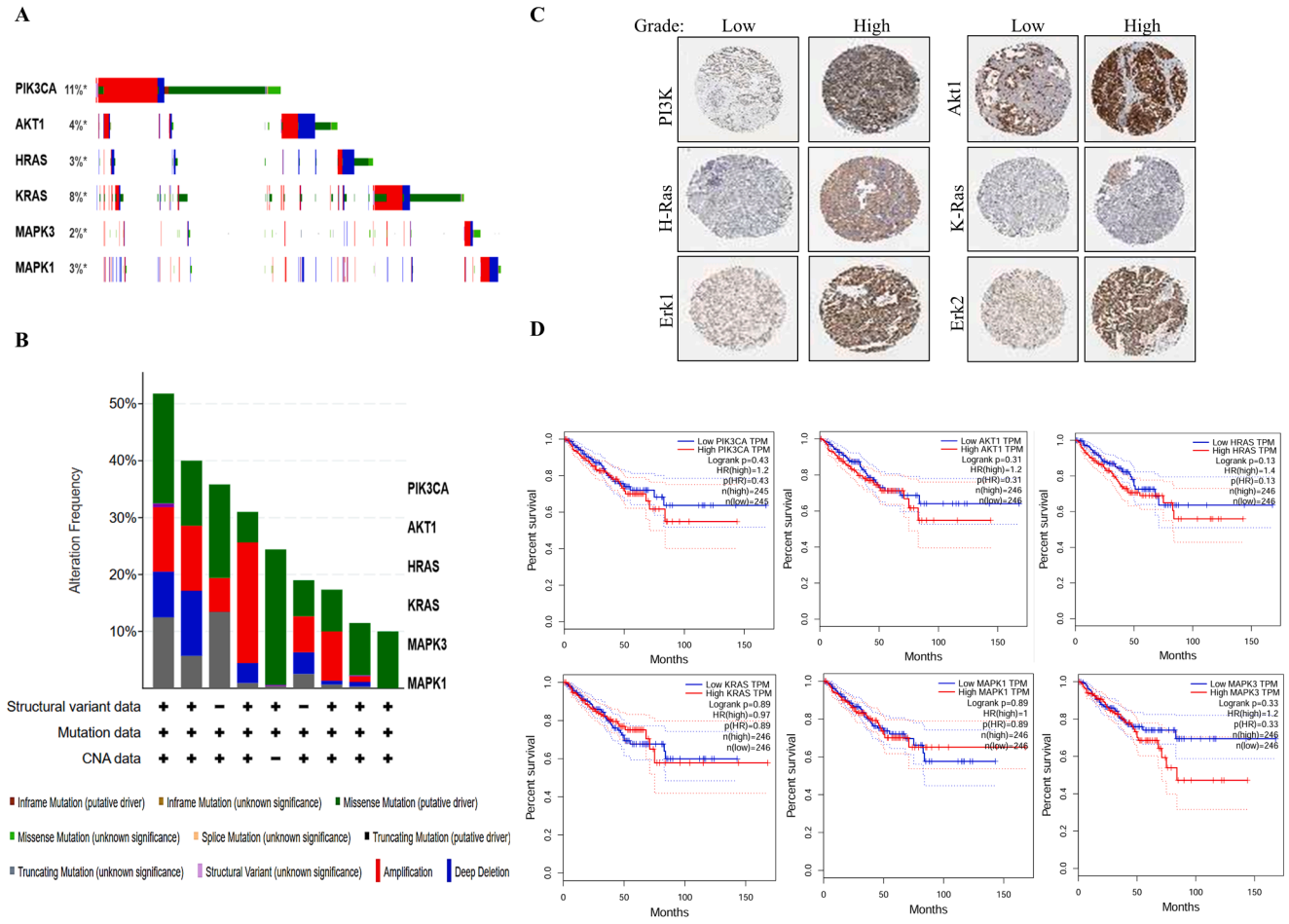

Fig. 5. Clinical significance of selected ComAR1 interacting proteins in PAC. A-B. TCGA data analysis of genetic alterations including amplification, mutation and deep deletion in designated genes from PAC patient samples were shown. **C.** Immunohistological examination of expression of indicated proteins in low- and high-grade PAC patient samples from Human Protein Atlas (HPA) database was shown. **D.** Survival analysis (disease-free) of PAC patients with low- and high expression of indicated proteins using Kaplan-Meier plotting was carried out.

significant genetic alterations including amplification, mutation and deletion (Fig. 5A-B). Immunohistochemical analyses from Human Protein Atlas (HPA) revealed that highly elevated expressions of PI3K, Akt1, H-Ras, Erk1/2 positively correlated with high grade PAC with lesser difference in expression of K-Ras among low- and high-grade PAC (Fig. 5C). Importantly, high expression of PI3K, Akt1, H-Ras, Erk1/2 positively correlated with low disease-free survival of PAC patients-implying their prognostic value in this lethal pathology. The binding poses of ComAR1 across crystal structures of 6GJB, 6SLG, 8PT3, 3D0E and 7LOF revealed conserved orientation within the active sites (Fig. 6A). ComAR1 consistently interacted with the surrounding residues with hydrogen bonds and π-π stacking. Notably, the Zn ion was found to be preserved in structures like 3D0E and 7LOF, contributing to metal coordination that enhanced binding affinity. Moreover, the core scaffold of ComAR1 maintained a stable fit within the binding pocket, supporting its role as a potent inhibitor scaffold.

3.5.2. *Molecular dynamics analyses of ComAR1 bound with substrates*

The root mean square derivation (RMSD) analysis over 200 ns molecular dynamics simulations provided insight into the structural stability of the top five ComAR1–protein complexes (Fig. 6B). The ComAR1-6GJB complex showed highest stability with backbone RMSD value plateauing at ~2.5 Å after initial equilibration phase and exhibited minimal fluctuations throughout the simulation- suggesting a well-maintained protein–ligand conformation. Similarly, ComAR1-6SLG complex maintained a stable trajectory, with RMSD value averaging at ~2.7 Å, further indicating a stable binding interaction. The ComAR1-8PT3 complex displayed moderate deviations, stabilizing at ~3.0 Å with occasional minor fluctuations, implying acceptable but less rigid structural integrity. In contrast, ComAR1-3D0E and ComAR1-7LOF complexes experienced higher RMSD variations, particularly ComAR1-7LOF complex, which reached up to 4.2 Å and showed frequent spikes, indicating possible conformational rearrangements or reduced binding stability. The elevated RMSD values for these complexes possibly suggest that as compared to its interaction with 6GJB and 6SLG, ComAR1 might weakly interact with 3D0E and 7LOF structures.

Root Mean Square Fluctuation (RMSF) is a parameter used in molecular dynamics to quantify the fluctuations of atomic positions over time, providing insights into the mobility and flexibility of different regions within a molecular structure [61]. Our RMSF analysis showed distinct flexibility patterns of 5 ComAR1-substrate complexes across their structural domains (Fig. 6C). 3D0E structure showed moderate flexibility throughout its sequence with notable high-flexibility regions around residues 250-270, reaching peak RMSF values of ~5 Å. 6GJB displayed relatively low overall flexibility with several discrete peaks of moderate amplitude (2-4 Å) distributed across the sequence,

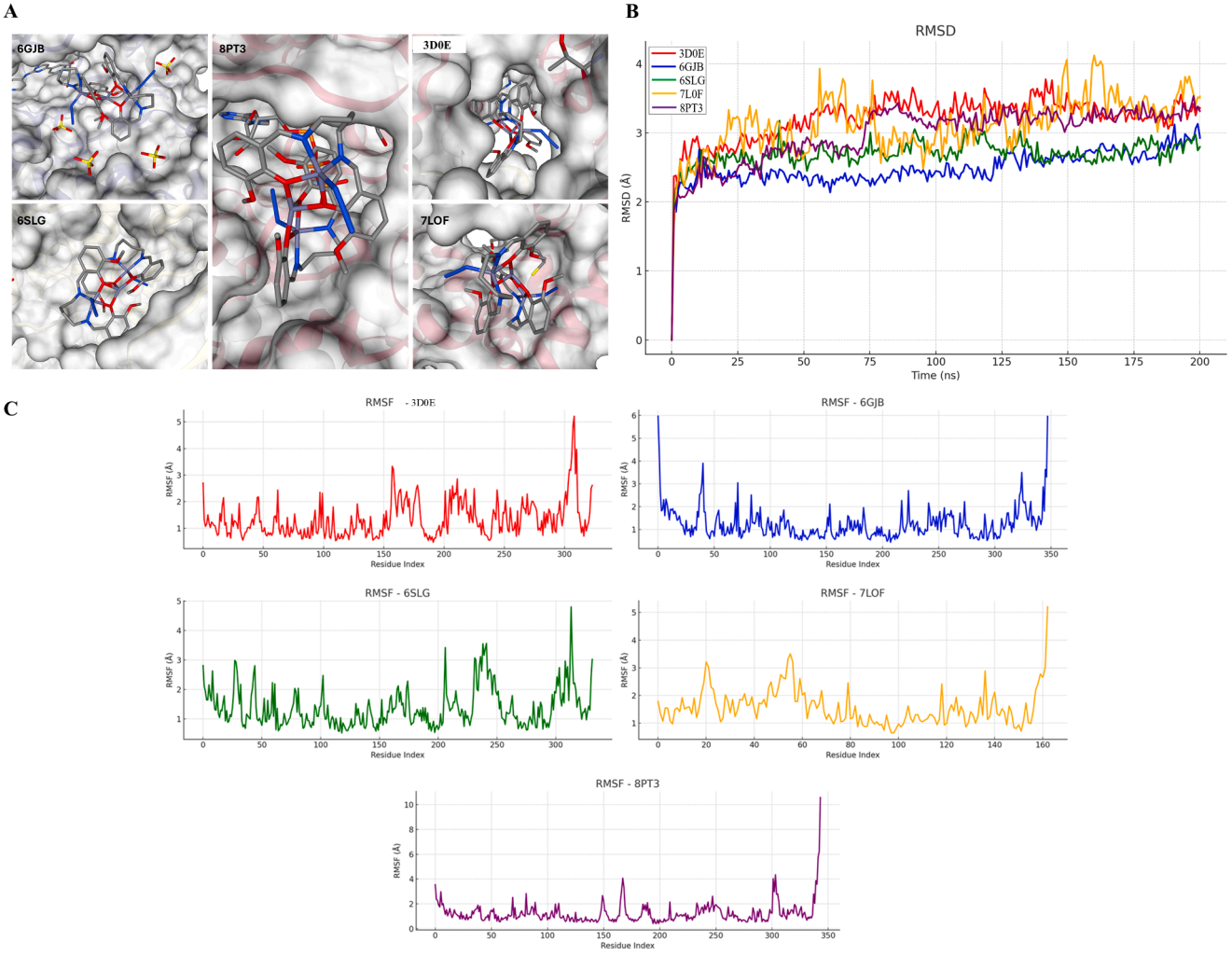

Fig. 6. Molecular docking, RMSD and RMSF analyses of ComAR1 and selected interacting proteins. A. The binding poses of ComAR1 across crystal structures of 6GJB (Erk2), 6SLG (Erk2 bound with ERK1/2 inhibitor AZD0364), 8PT3 (Erk2 covalently bound to RU77 cyclohexanone-based inhibitor), 3D0E (Akt2 bound with GSK690693) and 7LOF (HRAS bound to Monobody 12VC3) were shown. **B-C**. The root mean square derivation (RMSD) and root mean square fluctuation (RMSF) analyses of complexes between ComAR1 and indicated proteins were shown.

particularly around residues 50, 200, and 350. 6SLG structure demonstrated variable flexibility with significant fluctuations between 250 and 300 residue region, where RMSF values peaked at ~5 Å, suggesting a highly dynamic structure. 7LOF system, being shorter in sequence length (~160 residues), exhibited moderate flexibility with gradual increases toward the C-terminus, reaching maximum RMSF values at ~5 Å. 8PT3 structure revealed most dramatic flexibility profile, with extremely high fluctuations (>10 Å) occurring specifically around residue 320, indicating the presence of a highly disordered or mobile structural region, while maintaining relatively low flexibility (<2 Å) throughout the remaining sequence. These differential flexibility patterns suggested distinct functional and structural characteristics among the analyzed proteins, with regions of high RMSF values potentially corresponding to functionally important flexible loops, disordered domains, or allosteric sites.

Radius of gyration (RG) is an important indicator of protein structure compactness and can shed light on effect of factors contributing to ligand-substrate interactions [62]. Our RD analysis of proteins revealed distinct compactness profiles throughout the 200 ns molecular dynamics simulations (Fig. 7A). 3D0E maintained most compact conformation with a consistently low radius of gyration at ~20.5 Å, exhibiting minimal fluctuations with a stable, tightly folded structure. 6GJB structure displayed largest overall size with RG values ranging from ~21.7 to 22.3 Å, showing a gradual expansion over simulation time course, particularly after 150 ns. 6SLG and 8PT3 structures exhibited similar intermediate compactness levels, both maintaining relatively stable RG

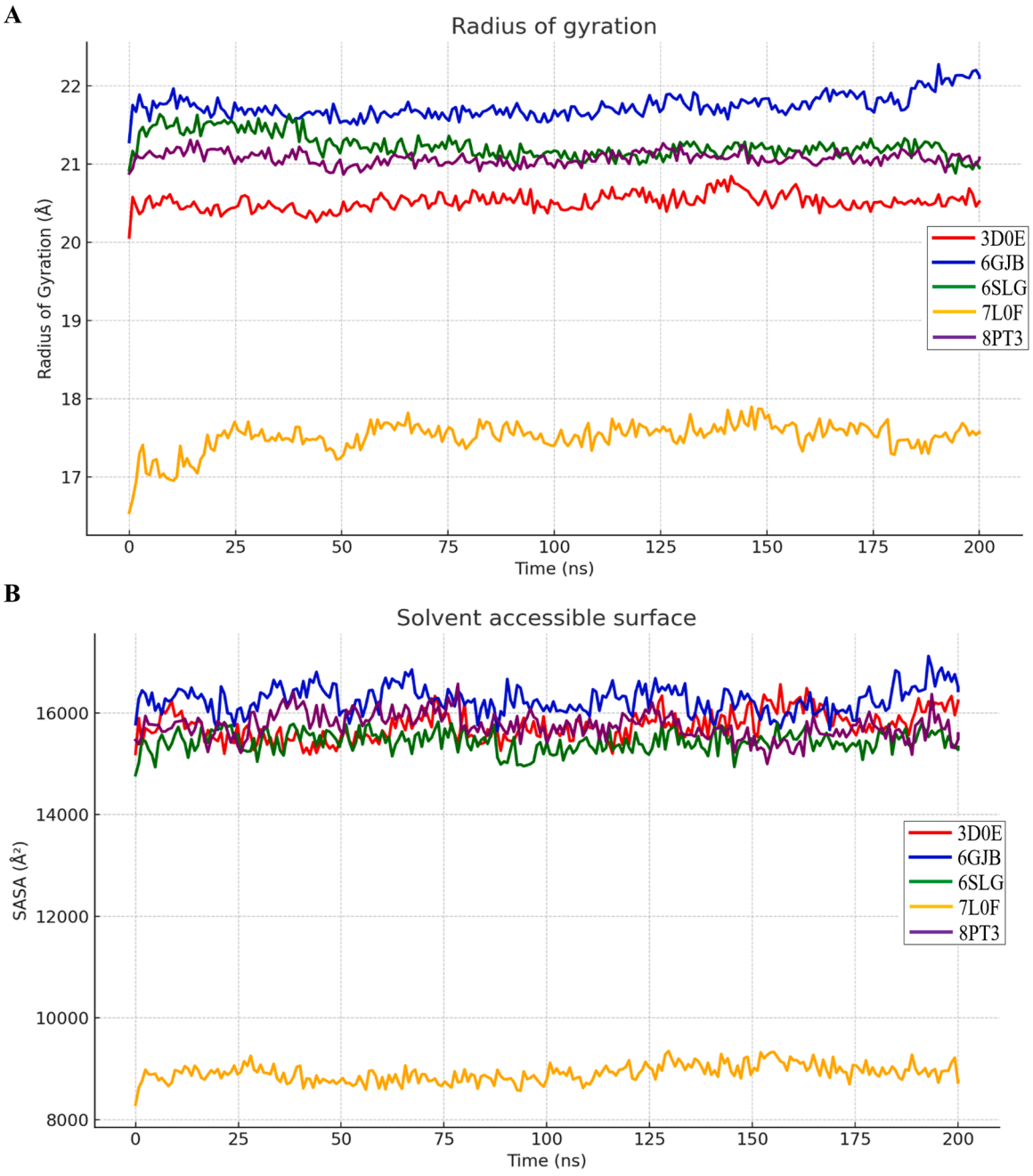

Fig. 7. Determination of radius of gyration and solvent accessible surface area (SASA) of complexes between ComAR1 and selected interacting proteins. A-B. The radii of gyration (RD) and solvent accessible surface area (SASA) analyses of ComAR1 across crystal structures of 6GJB (Erk2), 6SLG (Erk2 bound with ERK1/2 inhibitor AZD0364), 8PT3 (Erk2 covalently bound to RU77 cyclohexanone-based inhibitor), 3D0E (Akt2 bound with GSK690693) and 7LOF (HRAS bound to Monobody 12VC3) were shown.

values at ~21.0-21.5 Å with moderate fluctuations throughout the simulation period, indicating well-equilibrated structures with occasional conformational sampling. 7LOF, corresponding to its shorter sequence length, displayed smallest RG values ranging from 17.0 to 17.8 Å, with slight variations during the initial 50 ns followed by relative stability. These RG profiles suggested that while most systems achieved structural equilibration, the 6GJB system underwent continued structural changes, potentially indicating greater conformational flexibility or the presence of metastable states, whereas the other structures maintained their overall architectural integrity throughout the simulation timeframe.

Solvent accessible surface area (SASA) analysis is an essential parameter which provides important basis for understanding the molecular interactions, stability and function of proteins [63]. This analysis demonstrated distinct surface exposure patterns for five protein structures over 200 ns simulation period (Fig. 7B). 6GJB structure exhibited largest solvent-exposed surface area with values ranging from ~16,000 to 16,500 Å^2, showing moderate fluctuations throughout the simulation, which is consistent with its expanded conformation observed in the RG analysis. 3D0E, 6SLG, and 8PT3 displayed similar intermediate SASA values clustered around 15,500-16,000 Å^2, while maintaining relatively stable surface exposure profiles and overlapping trajectories-indicating comparable degrees of solvent accessibility despite their different sequence compositions. 7LOF which has shorter sequence length, showed the smallest solvent accessible surface area with values consistently around 9,000 Å^2 and minimal fluctuations-suggesting a compact and stable surface topology. These structures achieved equilibration within first 50 ns of simulation, as evidenced by the stabilization of SASA values, with subsequent fluctuations representing normal conformational sampling around equilibrium states. The correlation between SASA values and protein size, along with maintained stability across all structures, indicated that the proteins preserved their overall fold integrity while allowing for surface-accessible conformational dynamics typical of native protein behaviour in aqueous solution.

3.5.3. *Analysis of ComAR1-protein interactions and ADMET profiling of ComAR1*

Molecular recognition, a process of biological macromolecules exhibiting intra- and intermolecular interactions with high specificity and affinity to form a specific complex, constitutes the basis of all processes in living organisms and proteins realize their functions through binding to themselves or other molecules. Hence, detailed understanding of the protein–ligand interactions is therefore essential to understanding biology at the molecular level which will further facilitate the discovery, design, and development of drugs [64]. Interaction of ComAR1 with selected target proteins revealed distinct binding interaction profiles highlighting diverse molecular recognition mechanisms (Fig. 8A-E). The ComAR1-8PT3 (**Erk2** covalently bound to RU77 cyclohexanone-based inhibitor) complex (Fig. 8A) displayed unique interaction landscape with high hydrophobic interaction (purple) with

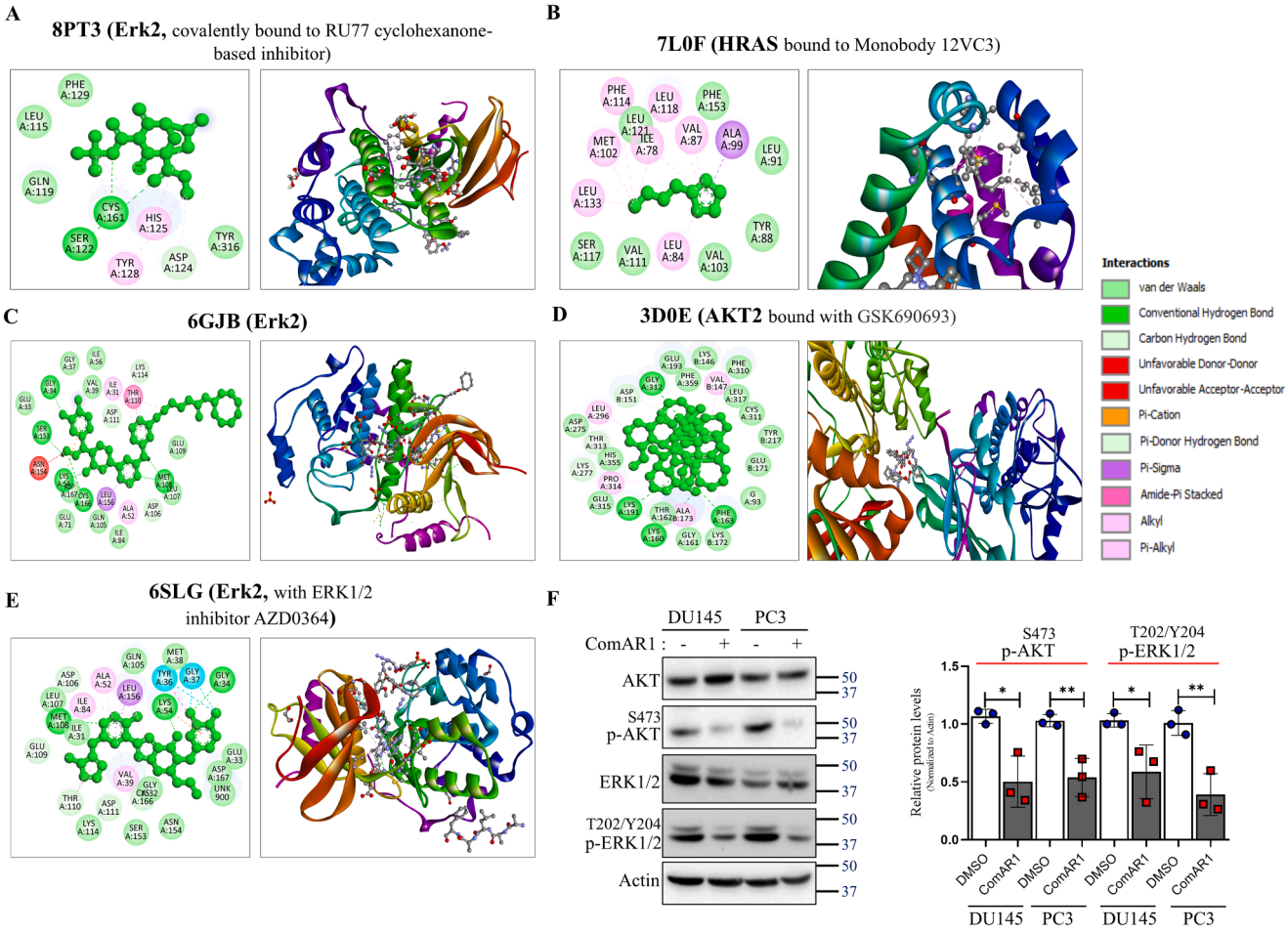

Fig. 8. Intermolecular interactions between ComAR1 and selected target proteins. ComAR1 exhibited several intermolecular interactions with amino acids of 8PT3 (**A**), 7L0F (**B**), 6GJB (**C**), 3D0E (**D**) and 6SLG (**E**) structures via different mechanisms including hydrogen bonds and ionic bridges (interaction legends, right panel). **F**. DU145 and PC3 cells were treated with ComAR1 as mentioned in Fig. 3A and expressions of indicated proteins were analyzed by Western blotting (left panel) and densitometric analysis of target protein expressions was performed (right panel). All values in the bar graphs were represented as mean ± SD of at least three independent experiments. A p value < 0.05 was considered significant (*, p <0.05; **, p <0.01). Actin served as loading control in F.

histidine and tyrosine at ~2.75 interaction fraction, complemented by moderate ionic interactions (magenta) and several weaker hydrophobic contacts- suggesting a predominantly hydrophobic binding environment with selective polar interaction sites. The ComAR1-7LOF (**HRAS** bound to Monobody 12VC3) complex (Fig. 8B) showed a balanced interaction profile featuring strong ionic interactions (magenta) reaching 1.75 interaction fraction, moderate hydrophobic contacts (purple and green), and notable water-mediated interactions (blue) which indicated a binding site capable of accommodating diverse chemical functionalities. ComAR1-6GJB (**Erk2**) complex (Fig. 8C) exhibited selective binding profile dominated by a single major hydrophobic interaction (green) reaching approximately 2.0 interaction fraction, accompanied by several moderate hydrophobic contacts (purple) ranging from 0.25-1.0, suggesting a binding site with pronounced hydrophobic character. ComAR1-3D0E complex (**AKT2** bound with GSK690693) (Fig. 8D) demonstrated most critical interaction pattern with multiple binding events distributed across various interaction types, predominant ionic (magenta) and several other interactions with significant peaks around 0.16-0.18 interaction fraction, complemented by moderate hydrophobic interactions (purple) and occasional hydrogen bonding (green) and water-mediated contacts (blue). Finally, ComAR1-6SLG (**Erk2,** with ERK1/2 inhibitor AZD0364) complex showed highly specific ligand recognition with one predominant ionic interaction (magenta) achieving an interaction fraction of ~2.5, representing the strongest single interaction observed across all complexes, with minimal contributions from other interaction types. These findings strongly suggested that mechanistically, ComAR1 might catalytically inactivate components of PI3K/AKT and Ras/MAPK/ERK pathways to exert its anti-cancer effect. Finally, to validate our *in-silico* results, we treated PAC cells DU145 and PC3 with 100 and 65 μg/ml of ComAR1 for 16 hours and analyzed the activation status of AKT and ERK1/2 by Western blotting. In line with the observations, our data showed that ComAR1 significantly dampened expression of phospho-AKT^{S473} and phospho-ERK1/2$^{T202/Y204}$ (Fig. 8F). As chemical absorption, distribution, metabolism, excretion and toxicity (ADMET) play crucial roles in the drug discovery, development and covers physicochemical properties of drugs, pH, solubility, drug metabolism and drug interactions [65], we performed ADMET analysis for ComAR1 to identify its suitability as a promising drug candidate for PAC (Table 4). Our results showed that Despite of a high molecular weight (993.01 g/mol), ComAR1 displayed good pharmacokinetic profiles and drug-likeness features. As it was not an inhibitor of major CYP450 isoforms (CYP1A2, CYP2C19, CYP2C9, CYP2D6, and CYP3A4), ComAR1 had minimized chance of drug-drug interactions. It also displayed promising bioavailability potential, as indicated by a bioavailability score of 0.11 and a PAINS-free profile, which indicated fewer false positives in screening assays. It was not hepatotoxic and permeable through the blood-brain barrier (BBB), properties consistently aligning with potential for peripheral targeting. ADMET analysis of ComAR1 passed Brenk filters for toxicophoric groups and had an acceptable synthetic accessibility (5.46). Although its solubility parameter was restricted, it was classified as moderately soluble by the SILICOS-IT model. Furthermore, its skin permeability was within an acceptable range. Taken together, our results indicated that ComAR1 can interact with elements of PI3K/AKT and Ras/MAPK/ERK pathways via distinct molecular recognition strategies including both electrostatic and hydrophobic interactions (Supplementary Fig. S9) to modulate the functions of these signalling circuits and could emerge as a potential therapeutic candidate for PAC.

4. ComAR1 suppresses BAD phosphorylation via PI3K/AKT and Ras/MAPK/ERK signalling cascades in PAC cells

Now that we have presented results that showed possible molecular interactions between ComAR1 and components of PI3K/AKT and Ras/MAPK/ERK pathways that collectively could translate into therapeutic potential of ComAR1 in PAC, we sought to uncover precise, underlying

Table 4
ADMET analysis of ComAR1.

Physiochemical Properties		**Pharmacokinetics**	
Formula	C40H48N10O8Zn3	GI absorption	Low
Molecular weight	993.01 g/mol	BBB permeant	No
No. heavy atoms	61	P-gp substrate	Yes
No. aromatic heavy atoms	24	CYP1A2 inhibitor	No
Fraction Csp3	0.30	CYP2C19 inhibitor	No
No. rotatable bonds	18	CYP2C9 inhibitor	No
No. H-bond acceptors	18	CYP2D6 inhibitor	No
No. H-bond donors	4	CYP3A4 inhibitor	No
Molar refractivity	221.05	Skin permeation (log k_p)	-6.36 cm/s
TPSA	242.06 A^2		
Lipophilicity		**Water Solubility**	
Log P_{aw} (iLOGP)	-146.89	Log *S* (ESOL)	-10.42
Log P_{aw} (XLOGP3)	8.45	Solubility	3.75e-08 mg/ml; 3.77e-11 mol/l
Log P_{aw} (WLOGP)	7.82	Class	Insoluble
Log P_{aw} (MLOGP)	-0.30	Log *S* (Ali)	-13.40
Log P_{aw} (SILICOS-IT)	4.92	Solubility	3.93e-11mg/ml; 3.95e-14mol/l
Consensus Log P_{aw}	-25.20	Class	Insoluble
		Log *S* (SILICOS-IT0	-5.78
		Solubility	1.64e-03mg/ml; 1.65e-06 mol/l
		Class	Moderately soluble
Drug likeness		**Medicinal Chemistry**	
Lipinski	No; 2 violations: MW>500, NarO>10	PAINS	1alert: azo_A
Ghose	No; 4 violations: MW>480, WLOGP>5.6, MR>130, atoms>70	Brenk	5 alerts: azido_group, diazo_group, heavy_metals, imine_1, quaternary _nitrogen_3
Veber	No; 2 violations: Rotors>10, TPSA>140	Leadlikeness	No; 3 violations: MW>350, Rotors>7, XLOGP3>3.5
Egan	No; 2 violations: WLOGP>5.88, TPSA>131.6	Synthetic accessibility	5.46
Muegge	No; 5 violations: MW>600, XLOGP3>5, TPSA>150, Rotors>15, H-acc>10		
Bioavailability	0.11		

mechanism of ComAR1-mediated anti-carcinogenic activity in PAC cells. First, we dissected the inhibitory effects of ComAR1 on both upstream and downstream members of PI3K/AKT and MAPK signalling circuits by treating DU145 and PC3 cells with 100 and 65 μg/ml of ComAR1, respectively for 16 hours followed by Western blot analysis of whole cell lysates. Our results showed that ComAR1 significantly suppressed activation of phospho-PI3K^{Y607}, phospho-AKT^{S473} in both PAC cells (Fig. 9A). Furthermore, degradation of Ras p21 and dampening of expression of phospho-ERK1/2$^{T202/Y204}$ were observed in ComAR1-treated DU145 and PC3 cells (Fig. 9B). Based on these results, we envisioned ComAR1 might possibly emerge as a dual inhibitor of these two clinically relevant signalling pathways in PAC. To further validate our results, we selectively targeted PI3K/AKT and MAPK signalling cascades with small molecule inhibitors and sought to understand if ComAR1 could phenocopy similar effects in PAC cells. Gefitinib is an inhibitor of EGFR tyrosine kinase, a member of HER kinase family whose aberrant activation in tumor cells leads to stimulation of Ras/Raf/MEK/MAPK and PI3K/AKT pathways; whereas, U0126 is a well-known ERK1/2 signalling inhibitor [34,66]. DU145 and PC3 cells were treated with 5μM of gefitinib or 10 μM of U0126 for 16 hours and activation status of these two pathways were analyzed by Western blotting. We observed that expressions of phospho-PI3K^{Y607}, phospho-AKT^{S473} and phospho-ERK1/2$^{T202/Y204}$ were dampened by gefitinib and U0126 suppressed expression of phospho-ERK1/2$^{T202/Y204}$ in PAC cells (Fig. 9C, Supplementary Fig. S10). Next, we treated PAC cells with 5 nM of dactolisib, a selective PI3K inhibitor for 16 hours and checked activation status of PI3K and AKT by immunoblotting. It was evident that dactolisib dampened expression of phospho-PI3K^{Y607} and phospho-AKT^{S473} in both DU145 and PC3 cells (Fig. 9C, Supplementary Fig. S10). Importantly, treatment of these cells with ComAR1 phenocopied the effects of gefitinib, U0126 and dactolisib-implying that ComAR1 dually inhibited Ras/Raf/MEK/MAPK and PI3K/AKT pathways in PAC cells.

To further strengthen our understanding of mechanistic role of ComAR1 as a novel therapeutic choice in PAC, we decided to identify any factor which could integrate signals from both PI3K/AKT and MAPK pathways to drive cancer cell proliferation, survival and potentially could be modulated by ComAR1. Previously we have shown that ComAR1 modulates expressions of Bcl-2 and Bax at both mRNA and protein levels (Fig. 4C-D). Recent reports suggest that several proteins including 4E-BP1 and BAD integrate signalling from PI3K/AKT and MEK/ERK pathways in tumors such as glioblastoma, and hence, development and clinical trials of dual inhibitors of AKT and ERK including ONC201 (dordaviprone) is underway [67,68]. Mechanistically, pro-survival signals from active PI3K/AKT and MEK/ERK pathways phosphorylate BAD at serine^{136} and serine^{112} residues, resulting in nuclear export, 14-3-3-mediated proteasomal degradation of BAD [69,70]. Hence, to corroborate our hypothesis that ComAR1 might dually inhibit both the pathways and modulate the function of BAD, we analyzed the

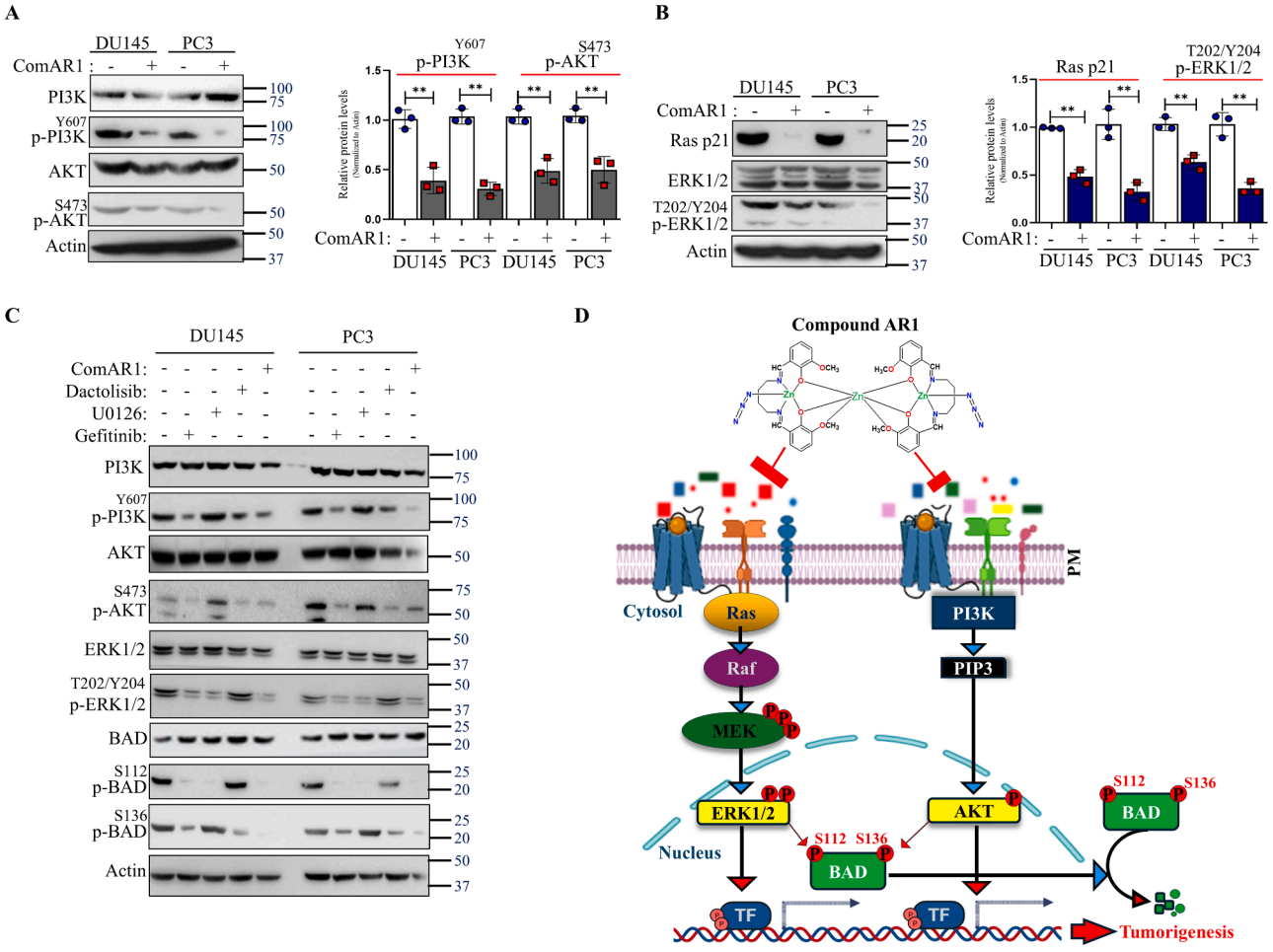

Fig. 9. ComAR1 dually dampens PI3K/AKT and MAPK/ERK signalling circuits to exert its anti-proliferative, anti-survival and anti-tumor effects on PAC cells. A-B. DU145 and PC3 cells were treated with ComAR1 as described in Fig. 3A and Western blot analysis was performed to assess the expressions of indicated proteins using designated antibodies. **C.** DU145 and PC3 cells were treated with 5 μM gefitinib, 10 μM U0126, 5 nM dactolisib or ComAR1 (according to the IC_{50} values of PAC cells) for 16 hours and expressions of indicated proteins were analyzed by immunoblotting using designated antibodies. **D.** A cartoon representing the molecular mechanism of ComAR1-induced anti-tumor activities in PAC cells was shown. All values in the bar graphs were represented as mean ± SD of at least three independent experiments. A p value < 0.05 was considered significant (**, $p < 0.01$). Actin served as loading control in C.

expression profile of phospho-BAD$^{S112/136}$ in gefitinib, U0126, dactolisib and ComAR1-treated PAC cells by immunoblotting. Our results demonstrated that selective inhibition of PI3K/AKT and MEK/ERK signalling using gefitinib, dactolisib or U0126 suppressed expressions of phospho-BAD^{S136} and phospho-BAD^{S112,} respectively, whereas ComAR1 inhibited both phosphorylation events (Fig. 9C). Taken together, our results indicated that ComAR1 inhibited PI3K/AKT and Ras/Raf/MEK/ERK signalling, stabilized pro-apoptotic BAD by suppressing its phosphorylation and induced its anti-cancer effects on PAC cells (Fig. 9D).

5. Discussion and conclusion

Despite of development of several therapeutic approaches including androgen receptor (AR) antagonists, targeted alpha therapy and immunotherapy, patient with prostate adenocarcinoma (PAC) frequently develop therapy-induced, castration-resistant metastatic PAC (mCRPC) which further exhibits neuroendocrine differentiation with high relapse rate and mortality [71]. Therefore, active research identifying new druggable targets and therapeutic options are underway worldwide. As Schiff base metal complexes significantly contribute to several biomedical applications including targeted therapy, precision medicine and drug delivery, in this report, we synthesized a novel zinc (II) trinuclear complex with tetradentate Schiff base ligand and azido ion (termed as Compound AR1 or ComAR1) in an aim to develop a novel therapeutic approach for improved management of PAC. ComAR1 significantly suppressed cancer-associated phenotypes including PAC cell migration, invasion and induced G0/G1 cell cycle arrest followed by cell membrane leakage, nuclear condensation followed by apoptosis. Furthermore, several *in-silico* analyses including molecular docking and simulations identified several key onco-drivers as putative targets of ComAR1 including MMPs, Jak and β-catenin. Interestingly, Akt2, H-Ras and Erk2 displayed most favourable docking score for ComAR1 and showed high probability of physically interaction with this compound via several modes such as H-bond and hydrophobic interactions. These proteins are components of pro-proliferative and pro-survival PI3K/AKT and Ras/Raf/MEK/ERK signalling pathways which are frequently dysregulated and aberrantly activated in PAC [60,72]. ADMET analysis of ComAR1 displayed excellent pharmacokinetic profiles and drug-likeness features including high degree of bioavailability, non-hepatotoxic and impermeability for blood-brain barrier. Mechanistically, ComAR1 treatment significantly dampened activation of PI3K, AKT and ERK1/2 as evidenced by suppressed expressions of phospho-PI3K^{Y607,} phospho-AKT^{S473} and phospho-ERK1/2$^{T202/Y204}$, respectively in DU145 and PC3 cells. Activated PI3K/AKT and Ras/MEK/ERK pathways crosstalk and integrate their pro-survival and anti-apoptotic effects by phosphorylating BAD at Ser^{136} and Ser^{112} residues, resulting in nuclear export and 14-3-3-mediated proteasomal degradation of BAD [67,73]. Importantly, ComAR1 dampened PI3K/AKT and Ras/MEK/ERK activation, stabilized BAD by inhibiting its phosphorylation and induced pro-apoptotic phenotypes in PAC cells. Our results identified ComAR1 as a potent dual inhibitor of these two signalling circuits and this novel compound could emerge as an improved therapeutic choice for PAC. Our findings are in line with the recent notion of development of several dual AKT and ERK inhibitors including ONC201 (dordaviprone) where it entered clinical trials in combination with other small molecules such as ixazomib, dexamethasone and cytarabine [68]. Therefore, ComAR1 can be therapeutically used alone or in combination with other drugs including enzalutamide for improved PAC patient outcomes. Despite of these concrete observations, this study contains few lacunas: 1) As PI3K/AKT and MAPK/ERK pathways intensively crosstalk with other signalling networks in both normal and tumor cells, clinical relevance of ComAR1 must be carefully examined in PAC and other cancer models where these two pathways are significantly dysregulated, 2) other specific ComAR1 targets must be identified and validated *in silico* and *in vitro* for improved translational and clinical outcomes and 3) therapeutic efficacy of ComAR1 should be validated using *in vivo* animal models in cancer. Nonetheless, our newly synthesized ComAR1 exhibited excellent anti-proliferative, anti-metastatic and pro-apoptotic activities in DU145 and PC3 cells, displayed promising pharmacokinetic profiles and drug-likeness features. Mechanistically, it dampened PI3K/AKT and Ras/MAPK/ERK signalling, stabilized pro-apoptotic BAD and exerted its therapeutic potential. Further research into identifying novel ComAR1 targets, developing its nanomedicine-based targeted delivery and clinical validation using *in vivo* cancer models are highly warranted.

Funding

This work was supported by Ramalingaswami Re-entry fellowship grant (BT/HRD/35/02/2006), Department of Biotechnology, Govt. of India, New Delhi awarded to AR and UGC (F.38-5/2009(SR)) and DST (SR/FT/CS-060/2009), New Delhi awarded to S. S.

CRediT authorship contribution statement

Abdul Wasai: Writing – review & editing, Writing – original draft, Visualization, Validation, Methodology, Investigation, Formal analysis. **Adhiraj Roy:** Writing – review & editing, Writing – original draft, Project administration, Funding acquisition, Formal analysis, Data curation, Conceptualization. **Mamata Barua:** Writing – original draft, Methodology, Investigation, Formal analysis. **Pameli Ghosh:** Writing – original draft, Methodology, Investigation, Formal analysis. **Anjali Saxena:** Writing – original draft, Methodology, Investigation, Formal analysis. **Yassir Boulaamane:** Writing – original draft, Methodology, Investigation, Formal analysis. **Nainee Goyal:** Writing – original draft, Methodology, Investigation, Formal analysis. **Anshuman Chandra:** Writing – original draft, Methodology, Investigation, Formal analysis. **Subrata Nath Koner:** Writing – original draft, Methodology, Investigation, Formal analysis. **Sandip Saha:** Writing – review & editing, Funding acquisition, Conceptualization. **Biswajit Saha:** Writing – review & editing, Project administration, Conceptualization. **Subrata Kumar Pore:** Writing – review & editing, Visualization, Project administration, Conceptualization. **Corrado Rizzoli:** Writing – review & editing, Conceptualization. **Supratim Mandal:** Writing – review & editing, Conceptualization.

Declaration of competing interest

The authors declare that there is no conflict of interest. Thank you for your consideration of our work. Please address all correspondence concerning this manuscript to me and feel free to correspond with me by e-mail (aroy2@amity.edu).

Sincerely yours
Dr. Adhiraj Roy
Associate Professor
Amity Institute of Molecular Medicine and Stem Cell Research
Amity University Uttar Pradesh
Sector 125, Noida
UP 201313, India.

Acknowledgment

This work was supported by Ramalingaswami Re-entry fellowship grant (BT/HRD/35/02/2006), Department of Biotechnology, Govt. of India, New Delhi awarded to AR and UGC (F.38-5/2009(SR)) and DST (SR/FT/CS-060/2009), New Delhi awarded to S. S. We are thankful to FIST program, Department of Science & Technology, Govt. of India for funding FACS facility in Amity Institute of Molecular Medicine & Stem Cell Research, Amity University Noida. We are grateful to Mr. Manoj Kumar Gupta, Amity University Noida, for excellent technical assistance for flow cytometry experiments.

Supplementary materials

Supplementary material associated with this article can be found, in the online version, at doi:10.1016/j.molstruc.2026.145636.

Data availability

Data will be made available on request.

References

[1] H. Sung, J. Ferlay, R.L. Siegel, M. Laversanne, I. Soerjomataram, A. Jemal, F. Bray, Global cancer statistics 2020: GLOBOCAN estimates of incidence and mortality worldwide for 36 cancers in 185 countries, CA. Cancer J. Clin. 0 (2021) 1–41.

[2] K. Fujita, N. Nonomura, Role of androgen receptor in prostate cancer: a review, World J. Men?S Heal. 37 (2019) 288–295.

[3] C. Dai, H. Heemers, N. Sharifi, Androgen signaling in prostate cancer, Cold Spring Harb, Perspect. Med. 7 (2017).

[4] B.Y. Shorning, M.S. Dass, M.J. Smalley, H.B. Pearson, The PI3K-AKT-mTOR Pathway and Prostate Cancer: At the Crossroads of AR, MAPK, and WNT Signaling, Int. J. Mol. Sci. 21 (2020) 1–47.

[5] C. Quicios-Dorado, E. Bolufer-Moragues, C. Gomis-Goti, R. Cabello-Benavente, P. J. Cannata-Ortiz, C. Gonzalez-Enguita, Aggressive variants of castration resistant prostate cancer (crpc): neuroendocrine prostate cancer, Arch. Esp. Urol. 71 (2018) 721–734.

[6] X. Shui, R. Xu, C. Zhang, H. Meng, J. Zhao, C. Shi, Advances in neuroendocrine prostate cancer research: From model construction to molecular network analyses, Lab. Investig. 102 (2021) 332–340, 2021 1024.

[7] B.J.B. Nelson, J.D. Andersson, F. Wuest, Targeted alpha therapy: progress in radionuclide production, radiochemistry, and applications, Pharmaceutics 13 (2020) 1–28.

[8] A. Morgenstern, C. Apostolidis, C. Kratochwil, M. Sathekge, L. Krolicki, F. Bruchertseifer, An Overview of Targeted Alpha Therapy with 225 Actinium and 213 Bismuth, Curr. Radiopharm. 11 (2018) 200–208.

[9] S.W. Ling, E. de Blois, E. Hooijman, A. van der Veldt, T. Brabander, Advances in 177Lu-PSMA and 225Ac-PSMA radionuclide therapy for metastatic castration-resistant prostate cancer, Pharmaceutics 14 (2022).

[10] J.L. Silberstein, S.K. Pal, B. Lewis, O. Sartor, Current clinical challenges in prostate cancer, Transl. Androl. Urol. 2 (2013) 122.

[11] D.A. Xavier, N. Srividhya, Synthesis and Study of Schiff base Ligands, IOSR J. Appl. Chem. 7 (2014) 06–15.

[12] C. Boulechfar, H. Ferkous, A. Delimi, A. Djedouani, A. Kahlouche, A. Boublia, A. S. Darwish, T. Lemaoui, R. Verma, Y. Benguerba, Schiff Bases and Their Metal Complexes: a review on the history, synthesis, and applications, Inorg. Chem. Commun. 150 (2023).

[13] V. Jagtap, B. Sathe, Synthesis and Characterization and In-vitro anti-inflammatory evaluation of new fluorobenzothiazole Schiff ' s base, (2016).

[14] K. Divya, G.M. Pinto, A.F. Pinto, Application of metal complexes of schiff bases as an antimicrobial drug: a review of recent works, Int. J. Curr. Pharm. Res. 9 (2017) 27.

[15] G. Matela, Schiff Bases and Complexes: A Review on Anti-Cancer Activity, Anticancer. Agents Med. Chem. 20 (2020) 1908–1917.

[16] G. Parkin, Synthetic Analogues Relevant to the Structure and Function of Zinc Enzymes, Chem. Rev. 104 (2004) 699–767.

[17] M. Barua, S. Bandyopadhyay, A. Wasai, M. Ghosh, I. Roy, P. Ghosh, S. Koner, C. Rizzoli, A. Roy, S. Saha, S. Mandal, A trinuclear Zn (II) schiff base dicyanamide complex attenuates bacterial biofilm formation by ROS generation and membrane damage and exhibits anticancer activity, Microb. Pathog. 188 (2024) 106548.

[18] S. Biswas, A. Wasai, M. Ghosh, C. Rizzoli, A. Roy, S. Saha, S. Mandal, A mononuclear N,N,N,O donor schiff base Cu(II) complex inhibits bacterial biofilm formation and promotes apoptosis and cell cycle arrest in prostate cancer cells, J. Inorg. Biochem. 247 (2023) 112314.

[19] M. Ghosh, S. Biswas, M. Roy, S. Biswas, P. Ghosh, S. Koner, S. Mandal, S. Saha, A trinuclear Zn(II) Schiff base azido compound: synthesis, structure and exploration of antimicrobial activity, New J. Chem. 45 (2021) 12296–12304.

[20] M. Ghosh, S. Saha, A. Banerjee, D. Schollmeyer, A. Sarkar, S. Banerjee, Azido bridged binuclear copper(ii) Schiff base compound: Synthesis, structure and electrical properties, New J. Chem. 43 (2019) 16255–16263.

[21] A.B. Deilami, M. Salehi, A. Arab, A. Amiri, Synthesis, crystal structure, electrochemical properties and DFT calculations of three new Zn(II), Ni(II) and Co (III) complexes based on 5-bromo-2-((allylimino)methyl)phenol Schiff-based ligand, Inorganica Chim. Acta 476 (2018) 93–100.

[22] K. Das, M. Dolai, S. Chatterjee, S. Konar, Synthesis, X-ray crystal structure and BVS calculation of Co(II) complex of pyrimidine derived Schiff base ligand: Approached by Hirshfeld surface analysis and TDDFT calculation, J. Mol. Struct. 1236 (2021) 130269.

[23] D. Bandyopadhyay, M. Layek, M. Fleck, R. Saha, C. Rizzoli, Synthesis, crystal structure and antibacterial activity of azido complexes of cobalt(III) containing heteroaromatic Schiff bases, Inorganica Chim. Acta 461 (2017) 174–182.

[24] W. Mertz, The essential trace elements, Science (80-.). 213 (1981) 1332–1338.

[25] A.I. Anzellotti, N.P. Farrell, Zinc metalloproteins as medicinal targets, Chem. Soc. Rev. 37 (2008) 1629–1651.

[26] D.S. Auld, The ins and outs of biological zinc sites, BioMetals 22 (2009) 141–148.

[27] M. Karmakar, S. Chattopadhyay, Synthesis, structure and nitroaromatic sensing ability of a trinuclear zinc complex with a reduced Schiff base ligand: Assessment of the ability of the ligand to sense zinc ion, Polyhedron 187 (2020) 114639.

[28] A. Majumder, C. Sarkar, I. Das, S. Sk, S. Bandyopadhyay, S. Mandal, M. Bera, Design, synthesis and evaluation of a series of zinc(II) complexes of anthracene-affixed multifunctional organic assembly as potential antibacterial and antibiofilm agents against methicillin-resistant staphylococcus aureus, ACS Appl. Mater. Interfaces 15 (2023) 22781–22804.

[29] V. Milosavljevic, Y. Haddad, M.A.M. Rodrigo, A. Moulick, H. Polanska, D. Hynek, Z. Heger, P. Kopel, V. Adam, The zinc-schiff base-novicidin complex as a potential prostate cancer therapy, PLoS One 11 (2016) e0163983.

[30] P.R. Spackman, M.J. Turner, J.J. McKinnon, S.K. Wolff, D.J. Grimwood, D. Jayatilaka, M.A. Spackman, CrystalExplorer: a program for Hirshfeld surface analysis, visualization and quantitative analysis of molecular crystals, J. Appl. Crystallogr. 54 (2021) 1006–1011.

[31] A. Roy, M.V. Veroli, S. Prasad, Q.J. Wang, Protein kinase D2 modulates cell cycle by stabilizing aurora a kinase at centrosomes, Mol. Cancer Res. (2018).

[32] S.M. Marques, S. Borko, O. Vavra, J. Dvorsky, P. Kohout, P. Kabourek, L. Hejtmanek, J. Damborsky, D. Bednar, Caver Web 20: analysis of tunnels and ligand transport in dynamic ensembles of proteins, Nucleic Acids Res 53 (2025) W132–W142.

[33] O. Trott, A.J. Olson, AutoDock Vina: improving the speed and accuracy of docking with a new scoring function, efficient optimization, and multithreading, J. Comput. Chem. 31 (2010) 455–461.

[34] K. Tyagi, A. Roy, S. Mandal, Pharmacological inhibition of protein kinase D suppresses epithelial ovarian cancer via MAPK/ERK1/2/Runx2 signalling axis, Cell. Signal. 110 (2023).

[35] S.M. Alonso Villela, H. Kraïem, B. Bouhaouala-Zahar, C. Bideaux, C.A. Aceves Lara, L. Fillaudeau, A protocol for recombinant protein quantification by densitometry, Microbiologyopen 9 (2020) e1027.

[36] W.A.Siddiqui Shehnaz, M.A. Raza, A. Ashraf, M. Ashfaq, M.N. Tahir, S. Niaz, Structure elucidation {single X-ray crystal diffraction studies, Hirshfeld surface analysis, DFT} and antibacterial studies of sulfonamide functionalized Schiff base copper (II) and zinc (II) complexes, J. Mol. Struct. 1295 (2024) 136603.

[37] D.C. Crans, M.L. Tarlton, C.C. McLauchlan, Trigonal Bipyramidal or Square Pyramidal Coordination Geometry? Investigating the Most Potent Geometry for Vanadium Phosphatase Inhibitors, Eur. J. Inorg. Chem. 2014 (2014) 4450–4468.

[38] J. Bernstein, M.C. Etter, L. Leiserowitz, The role of hydrogen bonding in molecular assemblies, Struct. Correl. 1 (2008) 431–507.

[39] H. Saluja, A. Mehanna, R. Panicucci, E. Atef, Hydrogen bonding: between strengthening the crystal packing and improving solubility of three haloperidol derivatives, Molecules 21 (2016) 719.

[40] L.C. Crowley, A.P. Scott, B.J. Marfell, J.A. Boughaba, G. Chojnowski, N. J. Waterhouse, Measuring cell death by propidium iodide uptake and flow cytometry, Cold Spring Harb. Protoc. 2016 (2016) 647–651.

[41] D.B. Kiselevsky, V.D. Samuilov, Permeability of the plasma membrane for propidium iodide and destruction of cell nuclei in the epidermis of pea leaves: the effect of polyelectrolytes and detergents, Moscow Univ. Biol. Sci. Bull. 74 (2019) 147–153.

[42] S.L. Regen, Membrane-disrupting molecules as therapeutic agents: a cautionary note, JACS Au 1 (2021) 3–7.

[43] N. Stylianou, M.L. Lehman, C. Wang, A.T. Fard, A. Rockstroh, L. Fazli, L. Jovanovic, M. Ward, M.C. Sadowski, A.S. Kashyap, R. Buttyan, M.E. Gleave, T. F. Westbrook, E.D. Williams, J.H. Gunter, C.C. Nelson, B.G. Hollier, A molecular portrait of epithelial–mesenchymal plasticity in prostate cancer associated with clinical outcome, Oncogene 38 (2018) 913–934, 2018 387.

[44] C.Y. Loh, J.Y. Chai, T.F. Tang, W.F. Wong, G. Sethi, M.K. Shanmugam, P.P. Chong, C.Y. Looi, The E-Cadherin and N-Cadherin Switch in Epithelial-to-Mesenchymal transition: signaling, therapeutic implications, and challenges, Cells 8 (2019).

[45] V. Odero-Marah, O. Hawsawi, V. Henderson, J. Sweeney, Epithelial-mesenchymal transition (EMT) and prostate cancer, Adv. Exp. Med. Biol. 1095 (2018) 101–110.

[46] B. Jingwen, L. Yaochen, Z. Guojun, Cell cycle regulation and anticancer drug discovery, Cancer Biol. Med. 14 (2017) 348.

[47] J.D. Liu, Y.J. Wang, C.H. Chen, C.F. Yu, L.C. Chen, J.K. Lin, Y.C. Liang, S.Y. Lin, Y. S. Ho, Molecular mechanisms of G0/G1 cell-cycle arrest and apoptosis induced by terfenadine in human cancer cells, Mol. Carcinog. 37 (2003) 39–50.

[48] M. Salehi, H. Piri, A. Farasat, B. Pakbin, N. Gheibi, Activation of apoptosis and G0/G1 cell cycle arrest along with inhibition of melanogenesis by humic acid and fulvic acid: BAX/BCL-2 and Tyr genes expression and evaluation of nanomechanical properties in A375 human melanoma cell line, (n.d.).

[49] S. Qian, Z. Wei, W. Yang, J. Huang, Y. Yang, J. Wang, The role of BCL-2 family proteins in regulating apoptosis and cancer therapy, Front. Oncol. 12 (2022) 985363.

[50] S. Toné, K. Sugimoto, K. Tanda, T. Suda, K. Uehira, H. Kanouchi, K. Samejima, Y. Minatogawa, W.C. Earnshaw, Three Distinct Stages of Apoptotic Nuclear Condensation Revealed by Time-Lapse Imaging, Biochemical and Electron Microscopy Analysis of Cell-Free Apoptosis, Exp. Cell Res. 313 (2007) 3635.

[51] D. Sahu, L.S. Rathor, S.D. Dwivedi, K. Shah, N.S. Chauhan, M.R. Singh, D. Singh, A review on molecular docking as an interpretative tool for molecular targets in disease management, Assay Drug Dev. Technol. 22 (2024) 40–50.

[52] P.C. Agu, C.A. Afiukwa, O.U. Orji, E.M. Ezeh, I.H. Ofoke, C.O. Ogbu, E.I. Ugwuja, P. M. Aja, Molecular docking as a tool for the discovery of molecular targets of nutraceuticals in diseases management, Sci. Rep. 13 (2023) 13398.

[53] M. Farhan, H. Wang, U. Gaur, P.J. Little, J. Xu, W. Zheng, FOXO signaling pathways as therapeutic targets in cancer, Int. J. Biol. Sci. 13 (2017) 815.

[54] J.M. Chan, S. Zaidi, J.R. Love, J.L. Zhao, M. Setty, K.M. Wadosky, A. Gopalan, Z. N. Choo, S. Persad, J. Choi, J. LaClair, K.E. Lawrence, O. Chaudhary, T. Xu, I. Masilionis, I. Linkov, S. Wang, C. Lee, A. Barlas, M.J. Morris, et al., Lineage plasticity in prostate cancer depends on JAK/STAT inflammatory signaling, Science (80-.) 377 (2022) 1180–1191.
[55] S. Zhu, J. He, L. Yin, J. Zhou, J. Lian, Y. Ren, X. Zhang, J. Yuan, G. Wang, X. Li, Matrix metalloproteinases targeting in prostate cancer, Urol. Oncol. Semin. Orig. Investig. 42 (2024) 275–287.
[56] A. Ali, G. Kulik, Signaling pathways that control apoptosis in prostate cancer, Cancers (Basel) 13 (2021) 937.
[57] S.P. Balk, K.E. Knudsen, AR, the cell cycle, and prostate cancer, Nucl. Recept. Signal. 6 (2008).
[58] B.Y. Shorning, M.S. Dass, M.J. Smalley, H.B. Pearson, The PI3K-AKT-mTOR pathway and prostate cancer: at the crossroads of AR, MAPK, and WNT Signaling, Int. J. Mol. Sci. 21 (2020) 4507.
[59] G. Rodríguez-Berriguete, B. Fraile, P. Martínez-Onsurbe, G. Olmedilla, R. Paniagua, M. Royuela, MAP Kinases and Prostate Cancer, J. Signal Transduct. 2012 (2011) 169170.
[60] Y. Numan, J. Zhao, S. Tang, Y. Zhang, Q. Zhang, B. Jovanovic, D.J. VanderWeele, A.K. Morgans, M. Cristofanilli, J. Yu, M.H.A. Hussain, Chemokine signaling and MAPK/ERK pathway for advanced prostate cancer treatment response, J. Clin. Oncol. 38 (2020). TPS275–TPS275.
[61] Y. Maruyama, R. Igarashi, Y. Ushiku, A. Mitsutake, Analysis of Protein Folding Simulation with Moving Root Mean Square Deviation, J. Chem. Inf. Model. 63 (2023) 1529–1541.
[62] M.Y. Lobanov, N.S. Bogatyreva, O.V. Galzitskaya, Radius of gyration as an indicator of protein structure compactness, Mol. Biol. 42 (2008) 623–628.
[63] S. Ali, M. Hassan, A. Islam, F. Ahmad, A review of methods available to estimate solvent-accessible surface areas of soluble proteins in the folded and unfolded states, Curr. Protein Pept. Sci. 15 (2014) 456–476.
[64] X. Du, Y. Li, Y.L. Xia, S.M. Ai, J. Liang, P. Sang, X.L. Ji, S.Q. Liu, Insights into protein–ligand interactions: mechanisms, models, and methods, Int. J. Mol. Sci., 17 (2016) 144.
[65] P. Gunwant Borole, A.N. Khadse, ADMET Predictor-An overview of prediction and evaluation of ADMET properties of drugs and chemicals, www.ijsdr.org Int. J. Sci. Dev. Res., 9 (2403).
[66] P. Wee, Z. Wang, Epidermal growth factor receptor cell proliferation signaling pathways, Cancers (Basel) 9 (2017) 52.
[67] Q. Ye, Q. She, Integration of AKT and ERK signaling pathways in cancer : biological and therapeutic implications, J. Pharmacol. Clin. Toxicol. 1 (2013) 2–5.
[68] Z. Cao, Q. Liao, M. Su, K. Huang, J. Jin, D. Cao, AKT and ERK dual inhibitors: the way forward? Cancer Lett. 459 (2019) 30–40.
[69] Y. Zhang, H. Liu, X. Liu, L. Lang, Gefitinib Induces Apoptosis in NSCLC Cells by Promoting Glutaminolysis and Inhibiting the MEK/ERK Signaling Pathway, Discov. Med. 36 (2024) 836.
[70] J. Hayakawa, M. Ohmichi, H. Kurachi, Y. Kanda, K. Hisamoto, Y. Nishio, K. Adachi, K. Tasaka, T. Kanzaki, Y. Murata, Inhibition of BAD phosphorylation either at serine 112 via extracellular signal-regulated protein kinase cascade or at serine 136 via Akt cascade sensitizes human ovarian cancer cells to cisplatin, Cancer Res. 60 (2000) 5988–5994.
[71] H. Beltran, F. Demichelis, Therapy considerations in neuroendocrine prostate cancer: what next? Endocr. Relat. Cancer 28 (2021) T67–T78.
[72] L. Chang, P.H. Graham, J. Ni, J. Hao, J. Bucci, P.J. Cozzi, Y. Li, Targeting PI3K/Akt/mTOR signaling pathway in the treatment of prostate cancer radioresistance, Crit. Rev. Oncol. Hematol. 96 (2015) 507–517.
[73] Y. Fu, S. Liu, S. Yin, W. Niu, W. Xiong, M. Tan, G. Li, M. Zhou, The reverse Warburg effect is likely to be an Achilles' heel of cancer that can be exploited for cancer therapy, Oncotarget 8 (2017) 57813–57825.

Glossary

ComAR1: Compound AR1;
PAC: Prostate Adenocarcinoma;
ADMET: Absorption, Distribution, Metabolism, Excretion, Toxicity;
EMT: Epithelial-to-mesenchymal Transition;
RMSD: Root Mean Square Derivation;
RMSF: Root Mean Square Fluctuation;
MD: Molecular Dynamics